

Imaging and time reversal in random media

Liliana Borcea* George Papanicolaou† Chrysoula Tsogka‡ James Berryman§

June 4, 2002

Abstract

We present a general method for estimating the location of small, well-separated scatterers in a randomly inhomogeneous environment using an active sensor array. The main features of this method are (i) an arrival time analysis of the echo received from the scatterers, (ii) a singular value decomposition of the array response matrix in the frequency domain, and (iii) the construction of an objective function in the time domain that is statistically stable and peaks on the scatterers. By statistically stable we mean here that the objective function is self-averaging over individual realizations of the medium. This is a new approach to array imaging that is motivated by time reversal in random media, analyzed in detail previously. It combines features from seismic imaging like arrival time analysis with frequency-domain signal subspace methodology like MULTiple SIGNAL Classification (MUSIC). We illustrate the theory with numerical simulations for ultrasound.

PACS numbers: 43.60.Gk, 43.60.Cg, 43.60.Rw

1 Array imaging

An active array of N transducers located at \mathbf{x}_p , for $p = 1, \dots, N$, probes an unknown medium containing $M < N$ small scatterers by emitting pulses and recording the back-scattered echos. To fix ideas, we consider a linear array where two adjacent point transducers are a distance $\lambda/2$ apart, where λ is the carrier (central) wavelength of the probing pulses. Such a setup ensures that the collection of transducers behaves like an array of aperture $a = (N - 1)\lambda/2$ and not like separate entities, while keeping the interference between the transducers at a minimum (Steinberg, 1983). Our aim is to identify the number M of scatterers and their location \mathbf{y}_p in a randomly inhomogeneous medium, in a regime where multipathing due to inhomogeneities is significant. Such a regime occurs, for example, when $\lambda \lesssim l \ll a \ll L$, where l is the correlation length of the random fluctuations of the wave speed and L is the range of the targets, as shown in Figure 1. In ultrasound imaging, the correlation length may be comparable to the central wavelength, which

*Computational and Applied Mathematics, MS 134, Rice University, 6100 Main Street, Houston, TX 77005-1892. (borcea@caam.rice.edu)

†Department of Mathematics, Stanford University, Stanford, CA 94305. (papanico@math.stanford.edu)

‡CNRS/LMA, 31 Chemin Joseph Aiguier, 13402 Marseille cedex 20, FRANCE, (tsogka@lma.cnrs-mrs.fr)

§Lawrence Livermore National Laboratories, P. O. Box 808 L-200, Livermore, CA 94551-9900. (berryman1@llnl.gov)

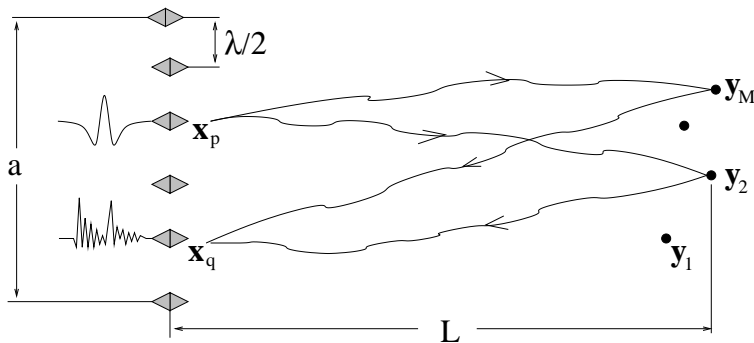


Figure 1: Array probing of a randomly inhomogeneous medium containing M small scatterers.

is typically 0.5mm, and propagation distances can be up to several hundreds of wavelengths. In such a regime, multipathing due to random inhomogeneities is important and must be taken into consideration.

1.1 The array response matrix

To image the targets we use the **response matrix** $(P_{pq}(t))$, obtained as follows. A pulse $f(t)$ is emitted from transducer p , located at \mathbf{x}_p , and the back-scattered returns, $P_{pq}(t)$, are recorded at \mathbf{x}_q , $q = 1, \dots, N$, for a sufficiently long time interval $(0, T)$. Probing of the medium is done by using all transducers, $p = 1, \dots, N$. The data collected is the response matrix $P(t) = (P_{pq}(t))$.

1.2 Types of arrays

Array probing can be done with many different types of arrays, transducers and recording devices. In ultrasound imaging the arrays are often linear, they may have as many as 100 or more transducers, and full response matrices can be measured and processed. In seismic imaging the arrays can be very large but they are mostly passive, that is, the array consists mostly of receivers and has few emitters. In sonar and radar the geometric layout of the arrays may depend on applications and it need not be linear or planar.

Large arrays of closely spaced transducers can be very effective in imaging but they are expensive, difficult to calibrate and to move, and they generate very large response matrices that require computationally intensive processing. However, imaging of acceptable quality can often be done with synthetic arrays, that is, with small arrays that are transported over the area to be imaged. They generate response matrices that have block-diagonal or near-diagonal form. In Synthetic Aperture Imaging (SAI), only the diagonal of the response matrix $P_{pp}(t)$ is measured. In Interferometric imaging, only the diagonal $P_{pp}(t)$ and one lower diagonal $P_{pp-1}(t)$ are measured, etc.

In very large arrays, synthetic or actual, the exact location of the transducers may not be known, so its imaging characteristics have to be calibrated using targets at known locations and with known scattering behavior. In this paper, we consider arrays with known transducer locations and full measured response matrices, although in some cases the methods we use work with less data.

1.3 Imaging strategies

Any reflection-based imaging method involves some form of back-propagation into the medium, or *time reversal*, of the fields measured on the array. This is because the back-propagated fields tend to focus on sharp reflectors in the medium. In *physical time reversal*, the back-propagating fields are emitted by the array into the real medium, which is unknown. In *virtual or computational time reversal*, the back-propagation is done numerically, in a fictitious, reference medium.

Physical time reversal has many applications in medicine, for example in the destruction of kidney stones (lithotripsy), as well as in the destruction of mines, in communications, and elsewhere (Fink, 1993; Fink, 1997; Kuperman et al., 1998; Song et al., 1999). Virtual time reversal is used mostly for imaging, as we discuss in this paper.

We may classify array imaging methods in three general categories: (a) time domain, broad-band methods that use mostly arrival time and/or amplitude information recorded by the array, (b) fixed frequency or narrow-band methods that use mostly differential phase information on the array, and (c) imaging methods based on intensity measurements. We consider here only the first two categories of imaging, which we call *coherent imaging* methods. Incoherent imaging uses only intensity measurements.

Time domain methods include broad-band Synthetic Aperture Imaging (Curlander and McDonough, 1991; Haykin et al., 1993), where only the diagonal $P_{pp}(t)$ of the response matrix is measured and used. The back-propagation of $P_{pp}(t)$ is done in a homogeneous medium, that is, we use arrival times computed in a homogeneous background (see Section 3.4). Time domain imaging methods are also used in exploration geophysics, where they are referred to as *migration*. In these applications, the measured array response matrices are very large and have very complex structure. The arrival time analysis is also very complicated because one cannot assume a uniform background medium. In Kirchhoff migration (Claerbout, 1985; Bleistein et al., 2001), the imaging is based on reference arrival times obtained by ray methods. Other migration methods back-propagate waves using various approximations, as in the one-way wave equation migration method (Claerbout, 1985; Bleistein et al., 2001). Narrow-band methods use differential phase information of the full array response matrix and they image by beam-forming (Curlander and McDonough, 1991; Haykin et al., 1993), or by fixed frequency subspace methods like MULTiple SIGNAL Classification (MUSIC) (Schmidt, 1979; Schmidt, 1986; Stoica and Moses, 1997). Least squares (maximum likelihood) direction of arrival estimation methods (Haykin et al., 1993) also use the full array response matrix in the frequency domain.

These imaging methods can be successfully used to locate the unknown targets, that is, to determine their number M and their spatial location \mathbf{x}_p , $p = 1, \dots, M$, when the background medium is deterministic and uniform. However, in the case of random media with significant multipathing, imaging is more difficult and conventional approaches such as Synthetic Aperture Imaging (SAI) (see Section 3.4) or subspace projection methods (MUSIC, see Section 3.3) perform very poorly. Statistical approaches, such as maximum likelihood, assume that the noise in the measured response matrix is additive and white. Such modeling is appropriate for instrument noise when signal to noise power is small, but it is not appropriate for dealing with stochastic effects arising from inhomogeneities in the medium that cause multipathing.

1.4 Imaging in random media

Since most imaging methods use virtual time reversal in some form, an important step towards successful imaging in random media is understanding physical time reversal and the role played by multipathing.

Physical time reversal has been explored with ultrasound (Fink, 1993; Fink, 1997; Prada et al., 1991; Prada et al., 1995; Prada et al., 1996; Fink et al., 2000), both with active sources and in echo mode, in underwater acoustics (Kuperman et al., 1998; Song et al., 1999), with numerical simulations (Blomgren et al., 2002; C.Tsogka and Papanicolaou, 2002) and with theoretical analysis (Blomgren et al., 2002; Clouet and Fouque, 1997; Dowling and Jackson, 1992). In physical time reversal the locations of the targets need not be known but sources at these locations must illuminate an array of transducers either actively or in echo mode. The signal recorded at the array is time reversed and re-emitted into the medium. Because of the time reversibility of the wave equation in a non absorbing medium, the back-propagated field focuses near the active targets. The array acts as a mirror that refocuses the time-reversed signals back onto the source from which they emanated. The focusing resolution is diffraction limited because of the finite aperture a of the array, as shown in Figure 2. In a homogeneous medium, the resolution in directions parallel to the array, the cross-range resolution, is $\lambda L/a$ (Born and Wolf, 1970). The resolution in the perpendicular direction, the range resolution, is $\lambda(L/a)^2 \gg \lambda L/a$ (Born and Wolf, 1970), when we have $L \gg a$. In randomly

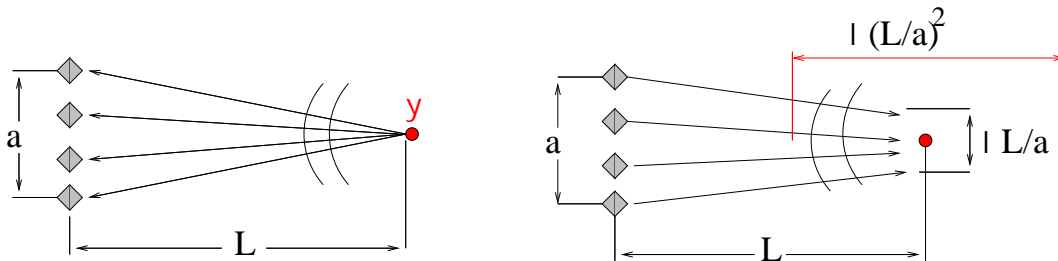


Figure 2: Time reversal in a homogeneous medium. A point source at \mathbf{y} emits a wave which is received at the array of aperture a , at a distance L from the source. The signal is time reversed and sent back into the medium. The focusing resolution in both range and cross-range is diffraction limited.

inhomogeneous media, the focusing resolution is much tighter (Fink, 1997; Blomgren et al., 2002). This phenomenon is called *super-resolution* and comes from multipathing caused by the random inhomogeneities. The array is like a lens with an effective aperture larger than its physical size, as indicated in Figure 3. Moreover, the time-reversed, back-propagated fields are *self-averaging* in the time domain. This means that super-resolution is *statistically stable*, that is, independent of the individual realizations of the random medium. A more detailed description of time reversal in random media is given in Section 2 and in (Blomgren et al., 2002).

In this paper we are interested in locating targets hidden in in a random medium, given the measured array response matrix $P(t)$. This is clearly different from physical time reversal. Nevertheless, the imaging methods that we propose are related to time reversal and therefore have its statistical stability. Our approach is a new, time resolved imaging method, where the unknown target locations are minimizers of an objective function that is statistically stable. The imaging method is based on the following two steps:

1. A statistically stable broad-band direction of arrival analysis which gives good cross-range resolution of the targets (Section 3.3).
2. An arrival time analysis which gives good range resolution of the targets (Section 3.5).

The combination of these two steps gives our estimates of the unknown target locations (Section 3.6).

Because the host medium has random fluctuations in the wave speed, the background medium is itself a source of scattered energy. We assume, however, that the targets are sufficiently larger and/or more reflective than the background fluctuations so that a clear distinction can be made between targets and background scatterers. However, we do assume that the medium fluctuations are weak (i.e., with standard deviation of the order of 5% or less) and we assume that $\lambda \lesssim l \ll a \ll L$. This is a regime where multipathing is significant even when the standard deviation of sound speed fluctuations is only a few percent (Papanicolaou et al., 2002). We do not consider strong multiple scattering that occurs in the random media studied in (Tourin et al., 2000).

In the next section we consider physical time reversal in a random medium and discuss super-resolution and statistical stability. We illustrate these phenomena with the results of numerical simulations.

In Section 3 we discuss imaging, beginning with a point-target model for the response matrix. We then introduce the array subspace analysis in Section 3.2, formulate robust time-domain direction-of-arrival estimators in Section 3.3 and show results of numerical simulations in Section 3.3.2. We also discuss briefly Synthetic Aperture Imaging (SAI) in Section 3.4 before estimating arrival times in Section 3.5. The Subspace Arrival Time (SAT) method uses time-domain direction-of-arrival estimation and arrival time estimates. It is introduced in Section 3.6 and performs very well when we have good arrival time estimates, as our numerical simulations show. When we do not have arrival time estimates, we can use a combination of direction-of-arrival estimation and SAI. This does not perform as well as SAT but is robust and considerably better than SAI. We end with a brief summary and conclusions.

2 Time reversal in random media

2.1 Super-resolution in time reversal

A short pulse $f(t)$ emanating from a point \mathbf{y} in the random medium illuminates the array of aperture a . The signal $\psi(\mathbf{x}_p, t)$ recorded at the array is synthesized from time harmonic waves as

$$\psi(\mathbf{x}_p, t) = \int_{-\infty}^{\infty} e^{-i\omega t} \hat{f}(\omega) \hat{G}(\mathbf{x}_p, \mathbf{y}, \omega) d\omega, \quad (2.1)$$

where the Fourier transform of the pulse is

$$\hat{f}(\omega) = \frac{1}{2\pi} \int_{-\infty}^{\infty} e^{i\omega t} f(t) dt. \quad (2.2)$$

We record the return signal for a long enough time so that there is negligible additional scattered energy. The time harmonic Green's function \hat{G} satisfies the reduced wave equation

$$\Delta \hat{G}(\mathbf{x}_p, \mathbf{y}, \omega) + \left(\frac{\omega}{c_0}\right)^2 n^2(\mathbf{x}) \hat{G}(\mathbf{x}_p, \mathbf{y}, \omega) = -\delta(\mathbf{x}_p - \mathbf{y}), \quad (2.3)$$

where c_0 is a reference speed and

$$n(\mathbf{x}) = \frac{c_0}{c(\mathbf{x})} \quad (2.4)$$

is the acoustic index of refraction of the medium with random sound speed $c(\mathbf{x})$.

The signal $\psi(\mathbf{x}_p, t)$ is time-reversed (conjugated in the Fourier domain) and re-emitted into the medium. The back-propagated field focuses near the illuminating point \mathbf{y} . To estimate the

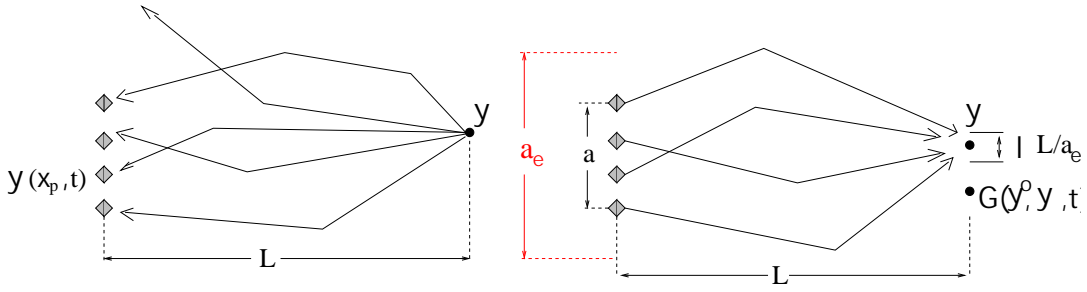


Figure 3: Time reversal in a random medium with significant multipathing. The array appears to have an effective aperture $a_e > a$ and the focusing of the back-propagated field is tighter than in a homogeneous medium.

focusing resolution we measure the amplitude of the field on a screen placed at distance L from the array, containing the source point \mathbf{y} and the observation points \mathbf{y}^o . The distance from the source to the first zero of the back-propagated amplitude, the first Fresnel zone, is the cross-range resolution in a homogeneous medium. In random media we fit the main lobe of the back-propagated amplitude with a Gaussian and take the estimated variance as the cross-range resolution (C.Tsogka and Papanicolaou, 2002). The time-reversed, back-propagated field at \mathbf{y}^o is

$$\Gamma(\mathbf{y}^o, \mathbf{y}, t) = \int_{-\infty}^{\infty} e^{-i\omega t} \hat{\Gamma}(\mathbf{y}^o, \mathbf{y}, \omega) d\omega, \quad (2.5)$$

where

$$\hat{\Gamma}(\mathbf{y}^o, \mathbf{y}, \omega) = \sum_{p=1}^N \overline{\hat{\psi}(\mathbf{x}_p, \omega)} \hat{G}(\mathbf{x}_p, \mathbf{y}^o, \omega) = \overline{\hat{f}(\omega)} \sum_{p=1}^N \hat{G}(\mathbf{x}_p, \mathbf{y}^o, \omega) \overline{\hat{G}(\mathbf{x}_p, \mathbf{y}, \omega)}. \quad (2.6)$$

In a homogeneous medium, $\Gamma(\mathbf{y}^o, \mathbf{y}, t)$ focuses near the source point \mathbf{y} , near the deterministic

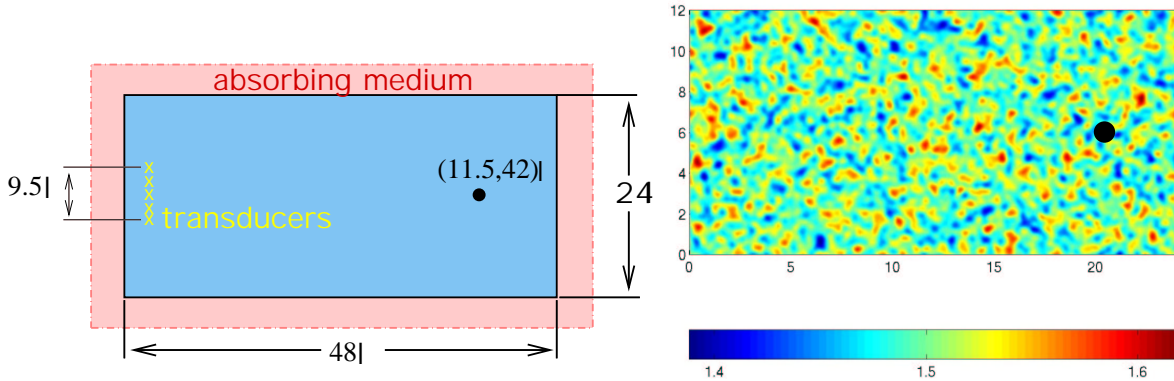


Figure 4: The computational setup. The dimensions of the problem are given in terms of the central wavelength $\lambda = 0.5\text{mm}$. The medium is considered to be infinite in all directions so in the numerical computations an absorbing layer surrounds the domain.

Figure 5: Typical realization of random sound speed $c(\mathbf{x})$. The target is shown as a large black dot \bullet . The units in the horizontal and vertical axes are mm and, in the color bar, km/sec. The standard deviation for this example is $s = 4.95\%$

arrival time, with cross-range resolution $\lambda L/a$, provided that $L \gg a$ (Born and Wolf, 1970). In a

randomly inhomogeneous medium, the focusing of $\Gamma(\mathbf{y}^o, \mathbf{y}, t)$ is tighter, as shown schematically in Figure 3. This is because the random inhomogeneities in the medium produce multipathing and the array appears to have an effective aperture a_e which can be much larger than a , its actual physical size. Therefore, the width $\lambda L/a_e$ of the focusing region is much smaller than in a homogeneous medium and we have *super-resolution*. The dependence of a_e on the random medium is analyzed in (Blomgren et al., 2002). From Figure 3 we can see that there will also be some diminution of the intensity of the signal recorded at the array because multipathing will scatter some energy away from it. This is of no great concern, however, since linearity allows us to amplify the signal $\psi(\mathbf{x}_p, t)$ before time-reversing and re-emitting it into the medium, assuming that instrument noise is small.

2.2 Simulations

We illustrate super-resolution for time reversal in random media with numerical simulations, using the setup shown in Figure 4. We solve the wave equation for the acoustic pressure field, in the time domain, in a medium with random sound speed $c(\mathbf{x})$ which has constant mean $c_0 = 1.5\text{km/s}$ and correlation length $l = 0.3\text{mm}$. The standard deviation of the fluctuations of $c(\mathbf{x})$ is denoted by s and in this case it varies between 0 and 5%. A typical realization of the randomly fluctuating sound speed is shown in Figure 5. The random fluctuations of the sound speed are generated numerically with Fourier series having suitably calibrated random amplitudes. The probing pulse

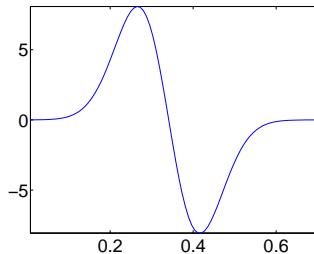


Figure 6: The probing pulse $f(t)$ given by (2.7). The horizontal axis is time t in micro seconds.

$$f(t) = -2\pi^2\nu^2 \left(t - \frac{1}{\nu} \right) e^{-\pi^2\nu^2(t-\frac{1}{\nu})^2}, \quad (2.7)$$

is shown in Figure 6. The central frequency is $\nu = 3\text{MHz}$, $\hat{f}(\omega)$ with $\omega = 2\pi\nu$, is supported over the band of frequencies $0.159 - 7.958\text{MHz}$ and the carrier wavelength is $\lambda = 0.5\text{mm}$.

We simulate an infinite medium by embedding the rectangular computational domain of size $24\lambda \times 48\lambda$ into a perfectly matched absorbing layer (cf. (Bérenger, 1994)). The source point is located at $\mathbf{y} = (11.5, 42)\lambda$, the array has aperture $a = 9.5\lambda$ and the transducers are located at $\mathbf{x}_p = (7 + (p-1)/2, 4)\lambda$, for $p = 1, \dots, 20$. In Figure 7, we show the back-propagated, time-reversed field $\Gamma(\mathbf{y}^o, \mathbf{y}, t)$ for all observation points \mathbf{y}^o in the computational domain, evaluated at the time it focuses on the source point \mathbf{y} . We show the results for two media. The left figure is for a homogeneous medium ($s = 0\%$) and the right for a random medium with standard deviation $s = 4.95\%$. Super-resolution results in a tighter compression of the pulse in the random medium. This can be seen more explicitly in Figure 8. We measure the width of the refocused wave amplitude at -6dB and find that the size of the focal spot is 2.3667mm for the homogeneous medium and 1.500mm for the random one, so the gain in this case is 36.62% .

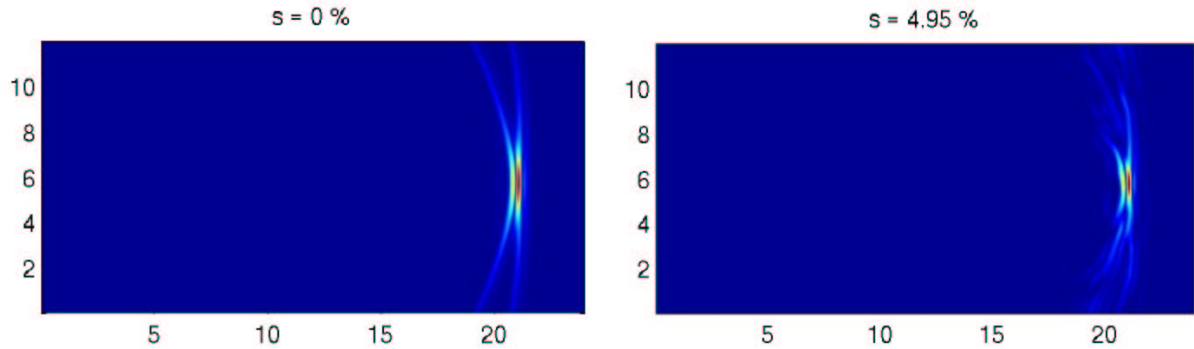


Figure 7: The re-focused field Γ shown as a function of range and cross-range in mm, at the time of re-focusing on the source point \mathbf{y} . The vertical array is 2mm from the left side and it has twenty transducers that are 0.25mm apart. Note the tighter focusing in the random medium.

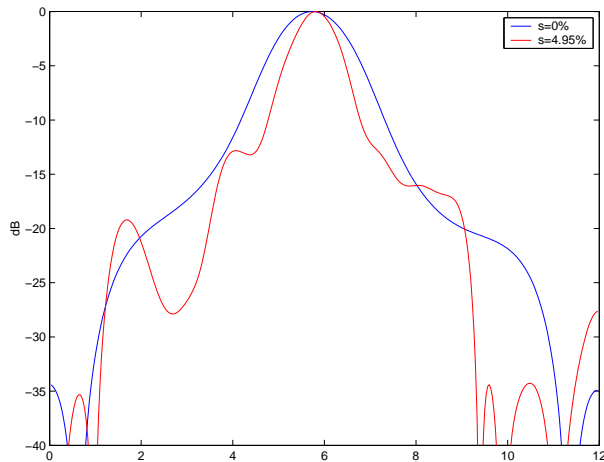


Figure 8: The re-focused field Γ at the range of the source shown as a function of cross-range (at the time of re-focusing on the source point \mathbf{y}). The field is normalized with respect to its maximum. The blue curve corresponds to the homogeneous medium and the red curve to the random one.

2.3 Statistical stability of time reversal

Experimental studies of time reversal (Fink, 1997; Kuperman et al., 1998) show a remarkable stability of the back-propagated, time-reversed field as it refocuses near the source point \mathbf{y} , in a variety of situations and without any averaging. We refer to this property as *self-averaging* of Γ , which is a time domain statistical phenomenon that does not occur for time-harmonic or narrow-band signals.

The key to self-averaging of Γ is the approximate statistical decorrelation of its Fourier components for different frequencies. This decorrelation holds in a regime where there is significant multipathing in the random medium. We have such a regime when the carrier wavelength λ and the correlations l of the sound speed fluctuations are short compared to propagation distances and the fluctuations are weak. Then

$$E \left\{ \hat{\Gamma}(\mathbf{y}^o, \mathbf{y}, \omega_1) \hat{\Gamma}(\mathbf{y}^o, \mathbf{y}, \omega_2) \right\} \approx E \left\{ \hat{\Gamma}(\mathbf{y}^o, \mathbf{y}, \omega_1) \right\} E \left\{ \hat{\Gamma}(\mathbf{y}^o, \mathbf{y}, \omega_2) \right\}, \quad \text{for } \omega_1 \neq \omega_2, \quad (2.8)$$

with $E\{\cdot\}$ being the expectation operator, and therefore

$$\begin{aligned}
E \{ \Gamma(\mathbf{y}^o, \mathbf{y}, t)^2 \} &= E \left\{ \int_{-\infty}^{\infty} d\omega_1 \int_{-\infty}^{\infty} d\omega_2 e^{-i(\omega_1 + \omega_2)t} \widehat{\Gamma}(\mathbf{y}^o, \mathbf{y}, \omega_1) \widehat{\Gamma}(\mathbf{y}^o, \mathbf{y}, \omega_2) \right\} \\
&\approx \int_{-\infty}^{\infty} d\omega_1 \int_{-\infty}^{\infty} d\omega_2 e^{-i(\omega_1 + \omega_2)t} E \left\{ \widehat{\Gamma}(\mathbf{y}^o, \mathbf{y}, \omega_1) \right\} E \left\{ \widehat{\Gamma}(\mathbf{y}^o, \mathbf{y}, \omega_2) \right\} \\
&= E^2 \{ \Gamma(\mathbf{y}^o, \mathbf{y}, t) \}.
\end{aligned} \tag{2.9}$$

From this result, we can easily prove that the probability of Γ differing significantly from its expected value is small. Using Chebyshev's inequality we see that for any small $\alpha > 0$,

$$\text{Prob}\{ | \Gamma(\mathbf{y}^o, \mathbf{y}, t) - E \{ \Gamma(\mathbf{y}^o, \mathbf{y}, t) \} | > \alpha \} \leq \frac{1}{\alpha^2} E \left\{ [\Gamma(\mathbf{y}^o, \mathbf{y}, t) - E \{ \Gamma(\mathbf{y}^o, \mathbf{y}, t) \}]^2 \right\} \approx 0,$$

which means that Γ is self-averaging.

In other words, in random media with significant multipathing, averaging over frequencies ω in the band of the probing pulse $f(t)$ is like averaging over realizations of the random medium and

$$\Gamma(\mathbf{y}^o, \mathbf{y}, t) \approx E \{ \Gamma(\mathbf{y}^o, \mathbf{y}, t) \}. \tag{2.10}$$

An analytic expression for $E \{ \Gamma(\mathbf{y}^o, \mathbf{y}, t) \}$ is given in (Blomgren et al., 2002) using the Green's function \widehat{G} in the paraxial approximation. It is shown there that $E \{ \Gamma(\mathbf{y}^o, \mathbf{y}, t) \}$ coincides with the back-propagated, time-reversed field in a homogeneous medium where the array has an effective aperture $a_e \gg a$. Therefore, $\Gamma(\mathbf{y}^o, \mathbf{y}, t)$ refocuses near the source point \mathbf{y} with cross-range resolution $\lambda L/a_e$, which is often much smaller than the diffraction limited resolution $\lambda L/a$.

We have done simulations of time reversal for many realizations of random media with standard deviation of the sound speed fluctuations $s \sim 5\%$ (Figure 7). Our numerical simulations show clearly the statistical stability of time reversal and the tighter focusing of the field Γ for different realizations of the random media.

3 Imaging

3.1 Point target model for the response matrix

To image the M unknown scatterers with an active array of transducers we measure the response matrix $(P_{pq}(t))$, $p, q = 1, \dots, N$, as explained in Section 1.1. We now describe a simple, point target model for $(P_{pq}(t))$, which is used in the analysis of our imaging algorithm.

When imaging M targets located at $\mathbf{y}_1, \dots, \mathbf{y}_M$, we will assume that, at frequency ω , $\widehat{P}(\omega) = (\widehat{P}_{pq}(\omega))$ is given by

$$\widehat{P}_{pq}(\omega) = \widehat{f}(\omega) \sum_{j=1}^M \widehat{\xi}_j(\omega) \widehat{G}(\mathbf{y}_j, \mathbf{x}_p, \omega) \widehat{G}(\mathbf{y}_j, \mathbf{x}_q, \omega), \quad p, q = 1, \dots, N, \tag{3.1}$$

where $\widehat{f}(\omega)$ is the Fourier transform of the probing pulse, \widehat{G} is the Green's function for the Helmholtz equation (2.3) in the random medium, and $\widehat{\xi}_j(\omega)$ is the scattering coefficient of the j^{th} target. Equivalently, the response matrix is a sum of outer products

$$\widehat{P}(\omega) = \widehat{f}(\omega) \sum_{j=1}^M \widehat{\xi}_j(\omega) \widehat{\mathbf{g}}(\mathbf{y}_j, \omega) \widehat{\mathbf{g}}^T(\mathbf{y}_j, \omega), \tag{3.2}$$

where T denotes transpose and where

$$\widehat{\mathbf{g}}(\mathbf{y}_j, \omega) = \begin{pmatrix} \widehat{G}(\mathbf{y}_j, \mathbf{x}_1, \omega) \\ \widehat{G}(\mathbf{y}_j, \mathbf{x}_2, \omega) \\ \vdots \\ \widehat{G}(\mathbf{y}_j, \mathbf{x}_N, \omega) \end{pmatrix}, \quad (3.3)$$

is the *illuminating* Green's vector onto the array, from the point \mathbf{y}_j . The main approximations made in (3.2) are the following:

- The targets are assumed to be isotropic point scatterers over the frequency band of the pulse.
- The transducers are also assumed to be isotropic point emitters and receivers.
- There is no multiple scattering between the unknown targets, which means that they are weak scatterers, or that they are well separated. The form of the response matrix \widehat{P} when there is multiple scattering between targets is given in the appendix. Multiple scattering of waves with background inhomogeneities is fully taken into account because the Green's function is random.

With these assumptions, (3.1) has the following interpretation. A point source at \mathbf{x}_p radiates a field with amplitude $\widehat{f}(\omega)$. This produces the field $\widehat{f}(\omega)\widehat{G}(\mathbf{y}_j, \mathbf{x}_p, \omega)$ at \mathbf{y}_j . Then, a scatterer acting as secondary source (from Huygen's principle) at \mathbf{y}_j , with this amplitude times its own scattering coefficient $\widehat{\xi}_j(\omega)$, radiates a field observed at \mathbf{x}_q , and given by (3.1).

Multipathing in the random medium is taken into account in (3.2) because we use the random Green's functions \widehat{G} . It should be kept in mind that (3.2) is a model that we use only in the theoretical analysis of the imaging algorithms. In our numerical simulations the response matrix $P(t) = (P_{pq}(t))$ is obtained by solving the full random wave equation in the presence of small inclusions that represent the targets.

3.2 Subspace analysis of the response matrix

We have pointed out that time reversal is a good way to look for the unknown target locations, that is, to image. However, having measured the response matrix $P(t)$, it is not clear what it is that we should time-reverse, in what medium to back-propagate it, and what to look for in the time-reversed, back-propagated space-time field. The Singular Value Decomposition (SVD) of the response matrix $\widehat{P}(\omega)$ in the frequency domain is the relevant tool (Prada et al., 1996; Devaney,). To understand why, we form the product

$$(\widehat{P}(\omega)\widehat{P}^H(\omega))_{pq} = \sum_{r=1}^N \widehat{P}_{pr}(\omega)\overline{\widehat{P}_{rq}(\omega)}. \quad (3.4)$$

Up to normalization by the scalar factor $\overline{\widehat{f}(\omega)}$ this has the following interpretation. A pulse $f(t)$ is emitted from the q^{th} transducer, the echos are recorded on the array, time-reversed and re-emitted from each transducer into the medium, and the echos are recorded again on the array. The resulting response matrix contains information obtained from probing the medium twice, the second time by time-reversal and back-propagation.

The eigenvectors and eigenvalues of the Hermitian matrix $\widehat{P}(\omega)\widehat{P}^H(\omega)$ have also a simple physical interpretation (Prada et al., 1996). They are the characteristic responses of the medium as

seen by the array at frequency ω . Suppose that the array emits a signal which at frequency ω has complex amplitudes equal to the components of one of the eigenvectors. The echos recorded at the array are time-reversed and re-emitted into the medium. After this double probing the response at the array is the eigenvector sent out, multiplied by the corresponding eigenvalue.

Given the singular value decomposition of the response matrix

$$\hat{P}(\omega) = \hat{U}(\omega)\Sigma(\omega)\hat{V}^H(\omega), \quad (3.5)$$

the eigenvectors of $\hat{P}(\omega)\hat{P}^H(\omega)$, denoted by $\hat{U}_r(\omega)$, for $r = 1, \dots, N$, are the columns of matrix $\hat{U}(\omega)$. The eigenvalues of $\hat{P}(\omega)\hat{P}^H(\omega)$ are $\sigma_r^2(\omega)$, $\sigma_r(\omega)$ being the singular values of $\hat{P}(\omega)$ that form the diagonal matrix $\Sigma(\omega)$. In our setup $\hat{P}(\omega)$ is complex symmetric but not Hermitian, so its left singular vectors $\hat{U}_r(\omega)$ are the complex conjugates of the right singular vectors $\hat{V}_r(\omega)$, for $r = 1, \dots, N$. We assume symmetry here for simplicity. All of our analysis nevertheless carries over to the non-symmetric case.

3.2.1 Application of the SVD

An immediate application of the SVD of the response matrix is the determination of the number of small targets. Suppose that only $M < N$ singular values of the measured response matrix $\hat{P}(\omega)$ are significant and the rest are zero or close to zero

$$\sigma_1(\omega) \geq \sigma_2(\omega) \geq \sigma_M(\omega) > \sigma_{M+1}(\omega) \approx \dots \sigma_N(\omega) \approx 0. \quad (3.6)$$

Based on the model (3.2) for the response matrix, this means that there must be M targets in the medium. If therefore the SVD of the array response matrix has no significant singular values over the band of frequencies of the probing pulse, then there are no detectable targets in the medium.

In general, the rank of the model response matrix $\hat{P}(\omega)$ is equal to the number of targets $M \leq N$, although there exist very special geometrical target configurations in homogeneous media that give a lower rank matrix (Devaney,). Such target configurations may be ignored in a random medium and for realistic arrays where the locations of sensors along a line or a plane are not exactly half a wavelength apart.

In Figure 9 we show the singular values $\sigma_j(\omega)$, for $j = 1, 2, 3$, computed from numerical simulations in the case of two targets embedded in homogeneous and random media. When the background is homogeneous only two singular values of the response matrix are significant, so we clearly detect the presence of two targets in the medium. In the case of random media with weak fluctuations ($s \leq 5\%$), more than two significant singular values may appear. However, the third and higher singular values are small for all frequencies and therefore we can consider them as noise and neglect them. As the fluctuations of the inhomogeneities increase the amplitude of the “noisy” significant singular values also increases and it appears as if more than two targets are in the random medium. This fact points to a natural limitation of this approach, since we cannot expect to detect targets in a medium when scattering from the random inhomogeneities is comparable to that from the targets.

Now, when there are detectable targets in the medium, the next step is to locate them. To do so, we can use the singular vectors of $\hat{P}(\omega)$. We remark that the first M left singular vectors $\hat{U}_1(\omega), \dots, \hat{U}_M(\omega)$ form an orthogonal basis of the M dimensional subspace of \mathbb{C}^N , spanned by the illuminating vectors at the target locations $\hat{\mathbf{g}}(\mathbf{y}_1, \omega), \dots, \hat{\mathbf{g}}(\mathbf{y}_M, \omega)$ while $\hat{U}_r(\omega)$, for $M+1 \leq r \leq N$, are orthogonal to this subspace. When the targets are sufficiently far apart from each other, destructive interference and the spatial decay of the Green’s functions imply that the inner product $\hat{\mathbf{g}}^H(\mathbf{y}_j, \omega) \hat{\mathbf{g}}(\mathbf{y}_h, \omega) \approx 0$ for $j \neq h$. In this case, we can associate with each target \mathbf{y}_j , $j = 1, \dots, M$,

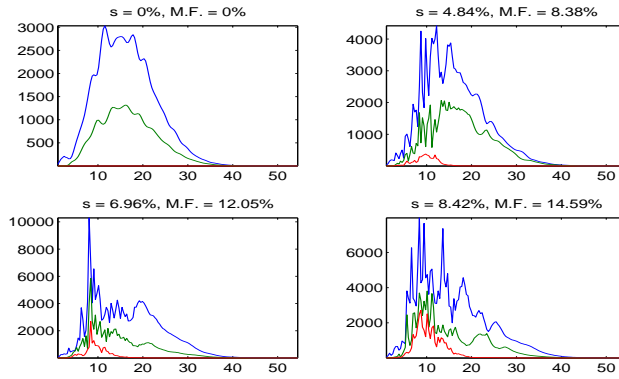


Figure 9: The first three singular values $\sigma_1(\omega)$, $\sigma_2(\omega)$ and $\sigma_3(\omega)$ from simulations with two targets in a random medium. The standard deviation s and maximum fluctuations (M.F.) are indicated on the top of each view. The horizontal axis is the radian frequency $\omega = 2\pi\nu$ with ν in MHz. Note crossing of singular values in the strongest random medium. Note also that in this medium it appears that there are more than two targets.

a nonzero singular value $\sigma_r(\omega)$ and the corresponding singular vector $\hat{\mathbf{U}}_r(\omega)$. In fact, the $\hat{\mathbf{U}}_r(\omega)$ are proportional to the illuminating vectors from the targets and we have

$$\hat{\mathbf{U}}_r(\omega) \approx e^{i\phi(\omega)} \frac{\hat{\mathbf{g}}(\mathbf{y}_j, \omega)}{|\hat{\mathbf{g}}(\mathbf{y}_j, \omega)|}, \quad \sigma_r(\omega) \approx |\hat{f}(\omega)| |\hat{\xi}_j(\omega)| |\hat{\mathbf{g}}(\mathbf{y}_j, \omega)|^2, \quad (3.7)$$

for some $1 \leq j \leq M$ and an arbitrary phase $\phi(\omega)$. In general, the targets will not always be sufficiently far apart and the approximation (3.7) will not hold. However, the rank of $\hat{P}(\omega)$ is M and the illuminating vectors $\hat{\mathbf{g}}(\mathbf{y}_1, \omega), \dots, \hat{\mathbf{g}}(\mathbf{y}_M, \omega)$ are linearly independent but not necessarily mutually orthogonal. The left singular vectors $\hat{\mathbf{U}}_r(\omega)$ are linear combinations of the illuminating vectors from the targets.

The problem is now how to use the singular value decomposition of the matrix $\hat{P}(\omega)$ over a band of frequencies of the probing pulse to image the M unknown targets. In the case of well separated targets we can image with *beam-forming*, at least in a homogeneous medium. We simply take the inner product of each singular vector $\hat{\mathbf{U}}_r(\omega)$ with the normalized illuminating vector at a test point \mathbf{y}^s in a homogeneous medium,

$$\hat{\mathbf{U}}_r^H(\omega) \frac{\hat{\mathbf{g}}_0(\mathbf{y}^s, \omega)}{|\hat{\mathbf{g}}_0(\mathbf{y}^s, \omega)|}. \quad (3.8)$$

At a fixed frequency this projection is a reasonable imager in a homogeneous medium, when the targets are not too close to the array. This is because by (3.7) the inner product (3.8) will be small unless \mathbf{y}^s is close to one of the targets.

However, in a random medium this inner product is wildly fluctuating from realization to realization and from frequency to frequency. We cannot integrate over frequency, as we did in time reversal, hoping to obtain a self-averaging quantity, for two reasons. The first one is that $\hat{\mathbf{U}}_r$ in (3.7) has an arbitrary frequency dependent phase $\phi(\omega)$ which comes from the way the SVD algorithm constructs the singular vectors. This problem is easy to fix by computing the singular vectors with the power method. The second reason is more serious and requires a different strategy, which we introduce in the next section. The problem is that the beam-forming inner product (3.8)

will never be self-averaging because the random Green's function in the singular vector in (3.7) is not compensated by a time-reversed one (the conjugated random Green's function) which cancels the large random phase that it has (see Section 2.3). Only functionals for which such large phases cancel can be self-averaging and therefore useful for imaging in random media. We discuss this further in Section 3.3.1.

3.3 Statistically stable broad-band direction of arrival estimation

An algorithm that leads to statistically stable imaging of the target locations can be constructed from the following observation:

- If the random vector $\widehat{\mathbf{g}}(\mathbf{y}^s, \omega)$ at a search point \mathbf{y}^s is orthogonal to the null-space of $\widehat{P}\widehat{P}^H(\omega)$ then \mathbf{y}^s must coincide with one of the target locations \mathbf{y}_j , for some $1 \leq j \leq M$.

We have already noted this property and now review it. The null-space of $\widehat{P}\widehat{P}^H(\omega)$ is spanned by the singular vectors $\widehat{\mathbf{U}}_r(\omega)$, for $M + 1 \leq r \leq N$, which are orthogonal to the subspace spanned by $\widehat{\mathbf{g}}(\mathbf{y}_1, \omega), \dots, \widehat{\mathbf{g}}(\mathbf{y}_M, \omega)$. The test illuminating vector $\widehat{\mathbf{g}}(\mathbf{y}^s, \omega)$ is orthogonal to the null-space of \widehat{P}^H , which is the same as that of $\widehat{P}\widehat{P}^H(\omega)$, if and only if it lies in the subspace spanned by $\widehat{\mathbf{g}}(\mathbf{y}_1, \omega), \dots, \widehat{\mathbf{g}}(\mathbf{y}_M, \omega)$. However, as explained in Section 3.2, the vectors $\widehat{\mathbf{g}}(\mathbf{y}^s, \omega), \widehat{\mathbf{g}}(\mathbf{y}_1, \omega), \dots, \widehat{\mathbf{g}}(\mathbf{y}_M, \omega)$ are linearly independent if $\mathbf{y}^s \neq \mathbf{y}_p$, for all $p = 1, \dots, M$. Therefore, if $\widehat{\mathbf{g}}(\mathbf{y}^s, \omega)$ is orthogonal to the null-space of $\widehat{P}\widehat{P}^H(\omega)$ then \mathbf{y}^s coincides with a target location \mathbf{y}_j , for some $1 \leq j \leq M$.

In a homogeneous medium the illuminating vector for a search point is known. Therefore projecting into the null-space of $\widehat{P}(\omega)$ at any fixed frequency will give a very good estimate of the target locations because they are exact zeros of the norm of the projection as a function of the search point \mathbf{y}^s (see (3.10)). This is, in fact, the well known MULTIPLE SIGNAL CLASSIFICATION (MUSIC) algorithm whose advantages over beam-forming and other target location methods is well known (Schmidt, 1979; Schmidt, 1986; Stoica and Moses, 1997).

When imaging in random media, however, the illuminating vector $\widehat{\mathbf{g}}(\mathbf{y}^s, \omega)$ at a search point \mathbf{y}^s is random and not known. The best we can do is use the known, deterministic illuminating vector $\widehat{\mathbf{g}}_0(\mathbf{y}, \omega)$ given at \mathbf{y}^s by

$$\widehat{\mathbf{g}}_0(\mathbf{y}^s, \omega) = \begin{pmatrix} \widehat{G}_0(\mathbf{y}^s, \mathbf{x}_1, \omega) \\ \widehat{G}_0(\mathbf{y}^s, \mathbf{x}_2, \omega) \\ \vdots \\ \widehat{G}_0(\mathbf{y}^s, \mathbf{x}_N, \omega) \end{pmatrix}, \quad (3.9)$$

where $\widehat{G}_0(\mathbf{y}^s, \mathbf{x}_j, \omega)$ is the deterministic two-point Green's function that solves (2.3) with $n(\mathbf{x}) \equiv 1$. To locate the targets we compute the projection $\mathcal{P}_N \widehat{\mathbf{g}}_0(\mathbf{y}, \omega)$ of $\widehat{\mathbf{g}}_0(\mathbf{y}^s, \omega)$ onto the null-space of $\widehat{P}\widehat{P}^H(\omega)$, given by

$$\mathcal{P}_N \widehat{\mathbf{g}}_0(\mathbf{y}^s, \omega) = \sum_{r=1}^M \left[\widehat{\mathbf{U}}_r^H(\omega) \widehat{\mathbf{g}}_0(\mathbf{y}^s, \omega) \right] \widehat{\mathbf{U}}_r(\omega) - \widehat{\mathbf{g}}_0(\mathbf{y}^s, \omega), \quad (3.10)$$

for each frequency in the support of the probing pulse $\widehat{f}(\omega)$.

In a deterministic medium the target locations \mathbf{y}_p , $p = 1, \dots, M$ are the zeros of $\|\mathcal{P}_N \widehat{\mathbf{g}}_0(\mathbf{y}^s, \omega)\|$ for any frequency. In a random medium we cannot expect this frequency by frequency projection to give a good estimate of the location of the targets because the deterministic illuminating vector $\widehat{\mathbf{g}}_0(\mathbf{y}^s, \omega)$ is, in general, quite different from the random one $\widehat{\mathbf{g}}(\mathbf{y}^s, \omega)$. In particular, at any fixed frequency ω , the replacement of the unknown illuminating vector $\widehat{\mathbf{g}}(\mathbf{y}^s, \omega)$ by the known one

$\widehat{\mathbf{g}}_0(\mathbf{y}^s, \omega)$ may be satisfactory for some realizations of the random medium but not for others. This means that imaging by projecting $\widehat{\mathbf{g}}_0(\mathbf{y}^s, \omega)$ onto the null-space of $\widehat{P}\widehat{P}^H(\omega)$ at a fixed frequency is **statistically unstable**. When, however, we take the inverse Fourier transform of this projected vector, suitably normalized, and evaluate it at an appropriate time, the averaging over frequencies ω produces a statistically stable functional that does provide information about the unknown targets in the random medium.

We now introduce, the statistically stable, time domain target imaging algorithm. We search for the targets one at a time. To find \mathbf{y}_j for some $1 \leq j \leq M$ we take a search point \mathbf{y}^s , calculate the illuminating vector $\widehat{\mathbf{g}}_o(\mathbf{y}^s, \omega)$, given by (3.9), and then compute its projection onto the subspace spanned by $\widehat{\mathbf{U}}_{M+1}(\omega), \dots, \widehat{\mathbf{U}}_N(\omega)$ as in (3.10). We normalize this projection by the singular value $\sigma_j(\omega)$ and we take the inverse Fourier transform to return to the time domain

$$\mathcal{F}^{(j)}(\mathbf{y}^s, t) = \int e^{-i\omega t} \sigma_j(\omega) \sum_{r=1}^M \left[\widehat{\mathbf{U}}_r^H(\omega) \widehat{\mathbf{g}}_o(\mathbf{y}^s, \omega) \right] \widehat{\mathbf{U}}_r(\omega) d\omega - \int e^{-i\omega t} \sigma_j(\omega) \widehat{\mathbf{g}}_o(\mathbf{y}^s, \omega) d\omega. \quad (3.11)$$

The normalization by the singular value $\sigma_j(\omega)$, which is given by (3.7) in the case of well separated targets, allows us to give a time reversal interpretation of the functionals $\mathcal{F}^{(j)}(\mathbf{y}^s, t)$ which are, therefore, self-averaging. We explain this in detail for a single target in Section 3.3.1.

Up to the normalization by $\sigma_j(\omega)$, the second term in (3.11) is the deterministic illuminating vector $\mathbf{g}_o(\mathbf{y}^s, t)$. The p -th component of this vector has a deterministic arrival time which is the travel time from the p^{th} transducer to the search point,

$$t_p(\mathbf{y}^s) = \frac{|\mathbf{x}_p - \mathbf{y}^s|}{c_0}. \quad (3.12)$$

It is natural, at least in homogeneous media, to evaluate the p^{th} component of $\mathcal{F}^{(j)}(\mathbf{y}, t)$ at time $t_p(\mathbf{y}^s)$. We then form the sum

$$\mathcal{G}^{(j)}(\mathbf{y}^s) = \sum_{p=1}^N \left(\mathcal{F}_p^{(j)}(\mathbf{y}^s, t_p(\mathbf{y}^s)) \right)^2 \quad (3.13)$$

and display the objective functional

$$\mathcal{R}(\mathbf{y}^s) = \sum_{j=1}^M \frac{\min_{\mathbf{y}^s} \mathcal{G}^{(j)}(\mathbf{y}^s)}{\mathcal{G}^{(j)}(\mathbf{y}^s)}, \quad (3.14)$$

for points \mathbf{y}^s in the target domain. The maxima of $\mathcal{R}(\mathbf{y}^s)$ are estimates of the target locations $\mathbf{y}_1, \dots, \mathbf{y}_M$.

In Section 3.3.2 we show results of numerical simulations for locating one or two targets in random media using this method (Figures 13 and 14). As these simulations indicate, and as we explain in Section 3.3.3, the imaging algorithm (3.14) gives a robust estimate of the the *Direction of Arrival* (DOA), or bearing, of scattered signals from the targets to the array. In homogeneous media we also get range estimation since the arrival times (3.12) are exact. In random media, however, the DOA estimator (3.14) does not give the range of the targets. In Section 3.3.3 we show that by using arrival time estimates from the data we can modify (3.13) so as to obtain good range estimates as well (Figure 17).

3.3.1 Imaging and time reversal

The functionals $\mathcal{F}^{(j)}(\mathbf{y}^s, t)$ defined by (3.11) are, up to normalization by the singular value $\sigma_j(\omega)$, just the time-domain projections into the null-space of $\widehat{P}(\omega)$, which is MUSIC in the time domain. The null-space projection is a good DOA estimator for narrow-band array probing in homogeneous media, considerably better than beam-forming (Schmidt, 1979; Schmidt, 1986), so extending it to the time domain is natural. Our understanding of time reversal in random media, discussed in Section 2, suggests an entirely different reason why suitably normalized MUSIC in the time domain is a good DOA estimator: *statistical stability*. This means that the estimator (3.14) is self-averaging because of multipathing (Blomgren et al., 2002) and therefore essentially independent of the random medium fluctuations. We now give a time reversal interpretation of $\mathcal{F}^{(j)}(\mathbf{y}^s, t)$ defined by (3.11). In Section 3.3.3 we discuss its sensitivity to arrival time estimation, which is then explored in several directions until Section 3.6 where we introduce the *Subspace Arrival Time* (SAT) estimator that is accurate and robust.

We consider for simplicity the case of a single target and drop the superscript (j) . Using the theoretical model (3.7) we can write (3.11) in the form

$$\mathcal{F}(\mathbf{y}^s, t) = \mathcal{B}(\mathbf{y}^s, t) - \mathcal{A}(\mathbf{y}^s, t), \quad (3.15)$$

with

$$\begin{aligned} \mathcal{A}(\mathbf{y}^s, t) &= \int_{-\infty}^{\infty} e^{-i\omega t} |\widehat{f}(\omega)| |\widehat{\xi}_1(\omega)| \widehat{\mathbf{g}}_0(\mathbf{y}^s, \omega) \sum_{p=1}^N \widehat{G}(\mathbf{y}_1, \mathbf{x}_p, \omega) \overline{\widehat{G}(\mathbf{y}_1, \mathbf{x}_p, \omega)} d\omega, \\ \mathcal{B}(\mathbf{y}^s, t) &= \int_{-\infty}^{\infty} e^{-i\omega t} |\widehat{f}(\omega)| |\widehat{\xi}_1(\omega)| \widehat{\mathbf{g}}(\mathbf{y}_1, \omega) \sum_{p=1}^N \widehat{G}_0(\mathbf{y}^s, \mathbf{x}_p, \omega) \overline{\widehat{G}(\mathbf{y}_1, \mathbf{x}_p, \omega)} d\omega. \end{aligned} \quad (3.16)$$

The self-averaging property of $\mathcal{F}(\mathbf{y}^s, t)$ is inherited from time reversal in random media because the random Green's functions in (3.16) appear in a way that is similar to the time-reversed, back-propagated field Γ in (2.6). In fact, both $\mathcal{A}(\mathbf{y}^s, t)$ and $\mathcal{B}(\mathbf{y}^s, t)$ have a time reversal interpretation as we shall explain. In general, self-averaging in the time domain occurs when large random phases in the Green's functions cancel or nearly cancel. This is the case with $\mathcal{A}(\mathbf{y}^s, t)$ and $\mathcal{B}(\mathbf{y}^s, t)$ because the random Green's functions appear in conjugate pairs. In $\mathcal{A}(\mathbf{y}^s, t)$ there is exact phase cancellation while in $\mathcal{B}(\mathbf{y}^s, t)$ the phase cancellation is approximate. The time domain stability comes from the approximate decorrelation of such quantities over different frequencies, as we discuss in Section 2.3.

In Figure 10 we illustrate the time reversal interpretation of $\mathcal{A}(\mathbf{y}^s, t)$ in three steps. First the unknown target sends to the array the pulse $|\widehat{f}(\omega)|$ weighted by the magnitude of the scattering strength $|\widehat{\xi}_1(\omega)|$. Then the echos received are time-reversed and back-propagated to the unknown point \mathbf{y}_1 , in the random medium. The field at \mathbf{y}_1 is

$$|\widehat{f}(\omega)| |\widehat{\xi}_1(\omega)| \sum_{p=1}^N \widehat{G}(\mathbf{y}_1, \mathbf{x}_p, \omega) \overline{\widehat{G}(\mathbf{y}_1, \mathbf{x}_p, \omega)}, \quad (3.17)$$

which is self-averaging in the time domain. In the third step we take the field at a search point \mathbf{y}^s and send it to the array in a fictitious homogeneous medium. We expect a large response at the array if \mathbf{y}^s is near \mathbf{y}_1 . Because of the self-averaging of time reversal in random media the components of $\mathcal{A}(\mathbf{y}^s, t)$ are self-averaging. In addition to this property, which is very important in

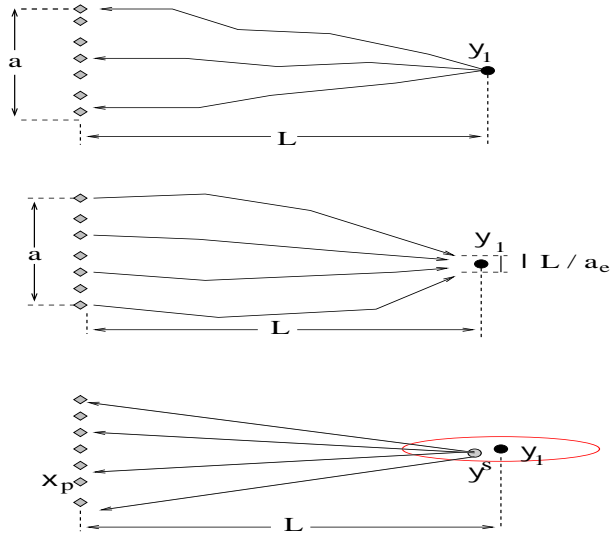


Figure 10: Time reversal interpretation of $\mathcal{A}(\mathbf{y}^s, t)$. The array is illuminated from the unknown location \mathbf{y}_1 in the random medium. The echos received at the array are time-reversed and re-emitted into the medium. They focus at \mathbf{y}_1 , with super-resolution. The field at the search point \mathbf{y}^s is then propagated to the array, in a fictitious, homogeneous medium. The p^{th} component of $\mathcal{A}(\mathbf{y}^s, t)$ is the signal at transducer \mathbf{x}_p and it is evaluated at the deterministic arrival time $t_p(\mathbf{y}^s) = |\mathbf{x}_p - \mathbf{y}^s| / c_0$.

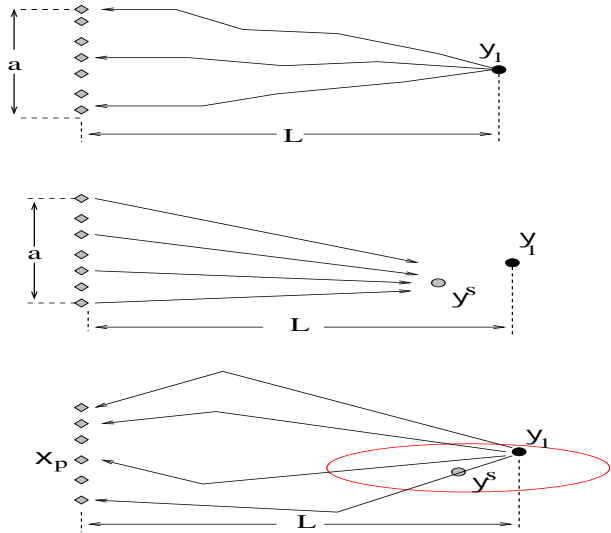


Figure 11: Time reversal interpretation of $\mathcal{B}(\mathbf{y}^s, t)$. The array is illuminated from the unknown location \mathbf{y}_1 in the random medium. The echos at the array are time-reversed and re-emitted in a fictitious homogeneous medium. In the third step the field at the unknown point \mathbf{y}_1 is send to the array in the random medium.

imaging, super-resolution plays a beneficial role in $\mathcal{A}(\mathbf{y}^s, t)$ as well. The search point \mathbf{y}^s , at a fixed range, has to be closer to the target \mathbf{y}_1 in order to produce significant illumination on the array.

In Figure 11 we illustrate the time reversal interpretation of $\mathcal{B}(\mathbf{y}^s, t)$, again in three steps. The first step is the same as for $\mathcal{A}(\mathbf{y}^s, t)$, that is we record at the array the echos received from the unknown location \mathbf{y}_1 in the random medium. Then we time-reverse and back-propagate to the search point \mathbf{y}^s in a fictitious homogeneous medium. The field at \mathbf{y}^s is

$$|\hat{f}(\omega)| |\hat{\xi}_1(\omega)| \sum_{p=1}^N \hat{G}_0(\mathbf{y}^s, \mathbf{x}_p, \omega) \overline{\hat{G}(\mathbf{y}_1, \mathbf{x}_p, \omega)}, \quad (3.18)$$

and it is not self-averaging. In the third step the field at the unknown point \mathbf{y}_1 is sent to the array of transducers in the random medium. Here again we expect a large response at the array if \mathbf{y}^s is near \mathbf{y}_1 . The components of $\mathcal{B}(\mathbf{y}^s, t)$ are self-averaging because in the last step we back-propagate in the random medium.

3.3.2 Simulations

We have computed array response matrices numerically for one-target and two-target configurations as shown in Figure 12. In both configurations we use the probing pulse given by (2.7), with the

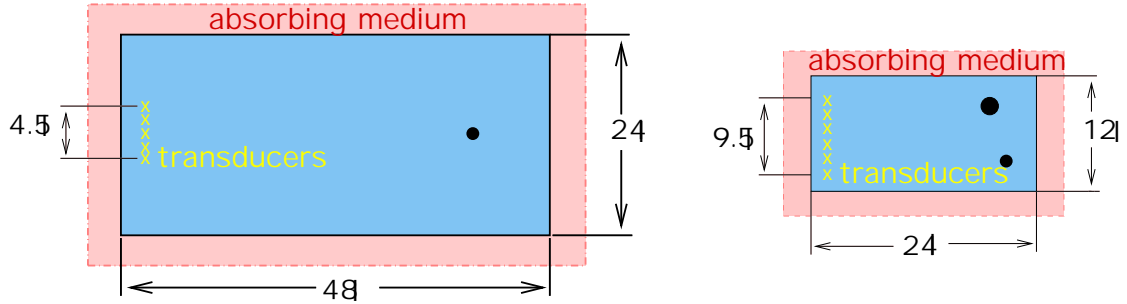


Figure 12: The setup for two numerical simulations. In the first case we have one target at $\mathbf{y}_1 = (11.5\lambda, 42\lambda)$ and the aperture of the array is 4.5λ . In the second case we have two targets, one bigger than the other. The larger target is located at $\mathbf{y}_1 = (8\lambda, 21\lambda)$ and the smaller one at $\mathbf{y}_2 = (4\lambda, 22\lambda)$. The aperture is 9.5λ .

same central frequency and frequency band. In the first simulation an array of aperture $a = 4.5\lambda$ is used to identify one target, which is located at $\mathbf{y}_1 = (11.5\lambda, 42\lambda)$. The array transducers are located at

$$\mathbf{x}_p = \left(9\lambda + (p-1)\frac{\lambda}{2}, 4\lambda \right), \text{ for } p = 1, \dots, 10.$$

In the second simulation we have two targets, one bigger and hence more reflective than the other. The larger target is located at $\mathbf{y}_1 = (8\lambda, 21\lambda)$ and the smaller one at $\mathbf{y}_2 = (4\lambda, 22\lambda)$. The array in this case has aperture $a = 9.5\lambda$ and the transducers are located at

$$\mathbf{x}_p = \left(7\lambda + (p-1)\frac{\lambda}{2}, 4\lambda \right), \text{ for } p = 1, \dots, 20.$$

The ambient medium is either homogeneous or random. The characteristics of the random media are the same as those in Section 2.2. The sound speed $c(\mathbf{x})$ has constant mean $c_0 = 1.5\text{km/s}$, correlation length $l = 0.3\text{mm}$ and standard deviation s between 1% and 5%.

We solve the wave equation with a numerical method based on the discretization of the mixed velocity-pressure formulation for acoustics. For the space discretization, we use a new finite element method (see (Bécache et al., 1997), (Bécache et al., 2000)), which is compatible with mass-lumping techniques (i.e., it leads to explicit time discretization schemes) and for the time discretization we use a centered 2nd order finite difference scheme. In the numerical simulations the targets are modeled by small squares. The size of the small target is $\lambda/30 \times \lambda/30$ and the size of the bigger one is $\lambda/15 \times \lambda/15$.

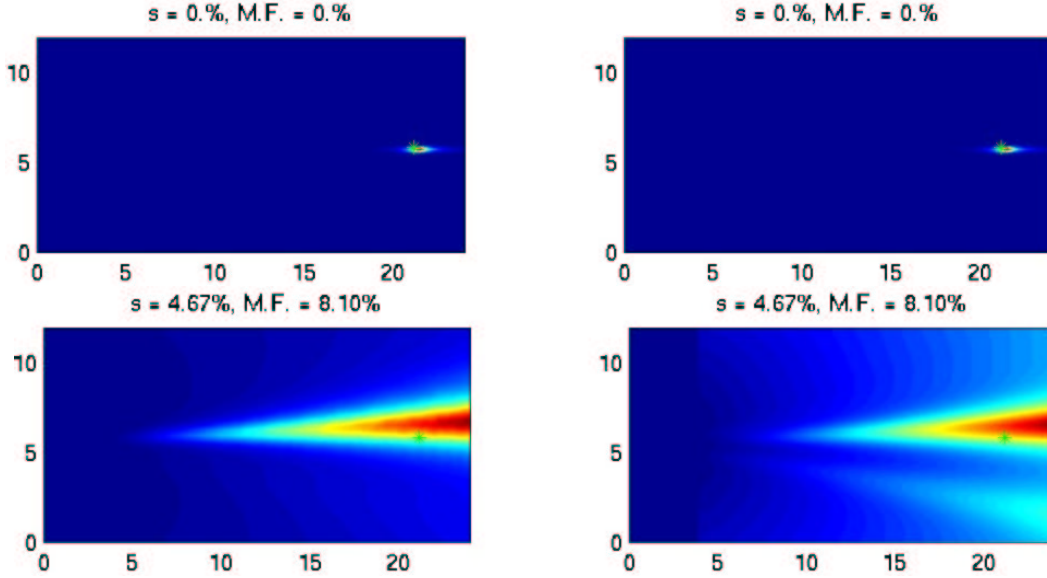


Figure 13: Direction of arrival estimation for one target in homogeneous and random media. On the left is the time domain estimation using (3.14) and on the right is fixed frequency MUSIC, at the central frequency of the pulse $\nu = 3\text{MHz}$. The target is the green star. The horizontal axis is range in mm and the vertical axis is cross-range in mm. The standard deviation s and the maximum fluctuations $M.F.$ are above each figure.

In Figures 13 and 14 we show the results obtained with the time domain estimation using (3.14) and a fixed frequency MUSIC estimation, at the central frequency of the pulse $\nu = 3\text{MHz}$. More precisely, we display the objective functional

$$\mathcal{R}_{\text{MUSIC}}(\mathbf{y}^s) = \frac{\min_{\mathbf{y}^s} \mathcal{G}_{\text{MUSIC}}(\mathbf{y}^s)}{\mathcal{G}(\mathbf{y}^s)}, \quad (3.19)$$

where $\mathcal{G}_{\text{MUSIC}}(\mathbf{y}^s)$ is computed by,

$$\mathcal{G}_{\text{MUSIC}}(\mathbf{y}^s) = |\mathcal{P}_N \hat{\mathbf{g}}_0(\mathbf{y}^s, \omega)|^2, \quad (3.20)$$

where $\mathcal{P}_N \hat{\mathbf{g}}_0(\mathbf{y}^s, \omega)$ is defined by (3.10) with $\omega = 2\pi\nu$. As we see in these figures both methods give very good results in homogeneous media. In random media the fixed frequency MUSIC estimation is not stable. It gives poor results for some realizations of the random medium and satisfactory for others. The time domain estimation is, however, statistically stable as expected. In the time domain we have a robust estimate of the cross-range, or direction of arrival, but range estimation in random media is not good at all. In the next Section 3.3.3 we use a simplified model for the random

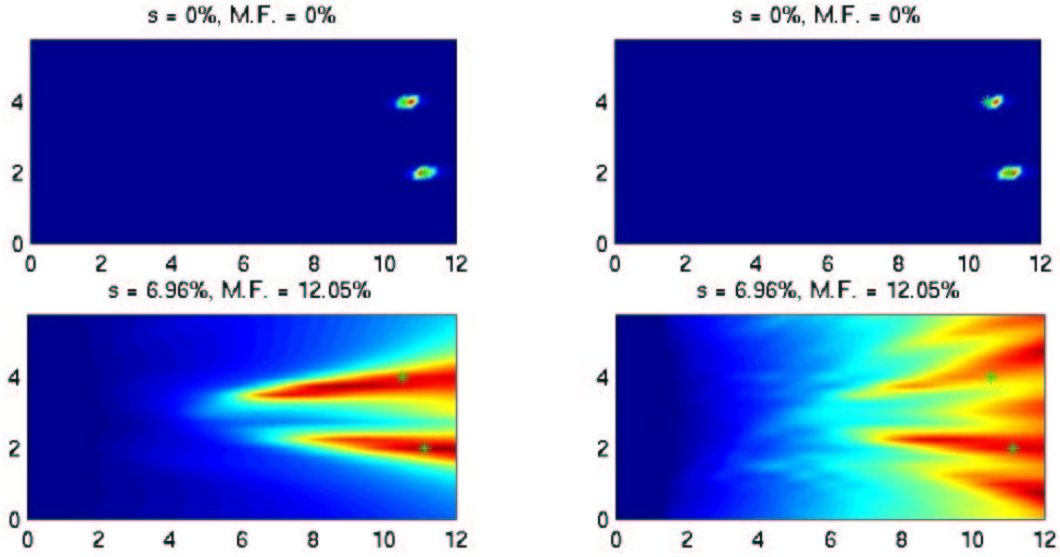


Figure 14: Same as Figure 13 with two targets.

Green's functions in order to explain the poor range estimation. It comes from the sensitivity of $\mathcal{F}^{(j)}(\mathbf{y}^s, t)$ to the arrival times used in it. The deterministic arrival times (3.12) are too crude. We show that by using good arrival time estimates from the data we can modify (3.13)-(3.14) so as to get good range estimates as well.

3.3.3 Sensitivity of imaging to arrival times

In Figures 13 and 14 the bottom left panel indicates clearly that MUSIC in the time domain, based on the functional $\mathcal{F}^{(j)}(\mathbf{y}^s, t)$ given by (3.11) and (3.14), is sensitive to what arrival times we use in $\mathcal{F}^{(j)}(\mathbf{y}^s, t)$. In this section we want to explain this sensitivity and to discuss the role that arrival times play in the behavior of the functional $\mathcal{F}^{(j)}(\mathbf{y}^s, t)$. MUSIC for narrow-band signals is a good direction of arrival (DOA) estimator (Schmidt, 1979; Schmidt, 1986) and this persists for broadband signals in the time domain, when we also have self-averaging. The price we pay for statistical stability is, however, sensitivity to arrival time information. This is an important trade-off in target location in random media that we now explain. We discuss it further in Section 3.4 in connection with synthetic aperture imaging and again in Section 3.6 where we combine direction of arrival estimation with arrival time analysis, which we call Subspace Arrival Time (SAT) analysis.

For simplicity we consider the case of one target ($j = 1$) located at \mathbf{y}_1 and write the q^{th} component of $\mathcal{F}^{(1)}(\mathbf{y}^s, t)$ using the Green's functions in the homogeneous, $\widehat{G}_o(\mathbf{y}_1, \mathbf{x}_p, \omega)$, and random media, $\widehat{G}(\mathbf{y}_1, \mathbf{x}_q, \omega)$, as follows

$$\begin{aligned} \mathcal{F}_q^{(1)}(\mathbf{y}^s, t) &= \sum_{p=1}^N \int_{-\infty}^{\infty} e^{-i\omega t} |\widehat{f}(\omega)| |\widehat{\xi}(\omega)| \left\{ \overline{\widehat{G}(\mathbf{y}_1, \mathbf{x}_p, \omega)} \widehat{G}_o(\mathbf{y}^s, \mathbf{x}_p, \omega) \widehat{G}(\mathbf{y}_1, \mathbf{x}_q, \omega) \right. \\ &\quad \left. - \overline{\widehat{G}(\mathbf{y}_1, \mathbf{x}_p, \omega)} \widehat{G}(\mathbf{y}_1, \mathbf{x}_p, \omega) \widehat{G}_o(\mathbf{y}^s, \mathbf{x}_q, \omega) \right\} d\omega. \end{aligned} \quad (3.21)$$

First we note that since $\mathcal{F}_q^{(1)}(\mathbf{y}^s, t)$ is self-averaging we may for the analysis replace the product $\widehat{G}(\mathbf{y}_1, \mathbf{x}_p, \omega) \widehat{G}(\mathbf{y}_1, \mathbf{x}_q, \omega)$ of two random Green's functions by its average. We can then approximate

this average by

$$E\{\overline{\widehat{G}(\mathbf{y}_1, \mathbf{x}_p, \omega)}\widehat{G}(\mathbf{y}_1, \mathbf{x}_q, \omega)\} \approx \frac{e^{-\beta(\omega)|x_p-x_q|^2}}{(4\pi)^2 r_p r_q} e^{-i\omega(\tilde{\tau}_p^{(1)}-\tilde{\tau}_q^{(1)})}, \quad (3.22)$$

where $r_p = |\mathbf{x}_p - \mathbf{y}_1|$ (and $r_p^s = |\mathbf{x}_p - \mathbf{y}^s|$ below), $p = 1, \dots, N$ are the distances from the p^{th} transducer to the target \mathbf{y}_1 (and the search point \mathbf{y}^s , respectively), and by $\tilde{\tau}_p^{(1)}$, for $p = 1, \dots, N$, we denote the travel time from the p^{th} transducer to the target in the random medium. These random travel times are estimated from the diagonal of the response matrix (see Section 3.5.1). This approximate expression for the average holds when the distance of the target from the array is large compared to its size ($a \ll L$), along with some other approximations (cf. (Blomgren et al., 2002)). The factor β depends on the frequency but we will assume it is constant since here we only want to give a qualitative analysis of the sensitivity of $\mathcal{F}_q^{(1)}(\mathbf{y}^s, t)$ to arrival times.

To continue our analysis of $\mathcal{F}_q^{(1)}(\mathbf{y}^s, t)$ we now simplify it by using (3.22) and doing the Fourier transform to get

$$\begin{aligned} \mathcal{F}_q^{(1)}(\mathbf{y}^s, t) \approx \mathcal{M}_q(\mathbf{y}^s, t) &= \frac{1}{(4\pi)^3} \sum_{p=1}^N \left\{ \frac{e^{-\beta|x_p-x_q|^2}}{r_p r_q r_p^s} f(t + \tilde{\tau}_p^{(1)} - \tilde{\tau}_q^{(1)} - t_p(\mathbf{y}^s)) \right. \\ &\quad \left. - \frac{1}{r_p^2 r_q^s} f(t - t_q(\mathbf{y}^s)) \right\}. \end{aligned} \quad (3.23)$$

We have also replaced $|\widehat{f}(\omega)|$ by $\widehat{f}(\omega)$ and set $|\widehat{\xi}(\omega)| = 1$. The times $t_p(\mathbf{y}^s)$, for $p = 1, \dots, N$, are the deterministic travel times given by (3.12). We form the functional

$$\mathcal{G}_M(\mathbf{y}^s) = \sum_{p=1}^N (\mathcal{M}_p(\mathbf{y}^s, t_p(\mathbf{y}^s)))^2 \quad (3.24)$$

and display

$$\mathcal{R}_M = \frac{\min_{\mathbf{y}^s} \mathcal{G}_M(\mathbf{y}^s)}{\mathcal{G}_M(\mathbf{y}^s)}, \quad (3.25)$$

at search points \mathbf{y}^s .

When evaluated at time $t = t_q(\mathbf{y}^s)$, (3.23) becomes,

$$\mathcal{M}_q(\mathbf{y}^s, t_q(\mathbf{y}^s)) = \frac{1}{(4\pi)^3} \sum_{p=1}^N \left[\frac{e^{-\beta|x_p-x_q|^2}}{r_p r_q r_p^s} f(\tilde{\tau}_p^{(1)} - \tilde{\tau}_q^{(1)} - (t_p(\mathbf{y}^s) - t_q(\mathbf{y}^s))) - \frac{1}{r_p^2 r_q^s} f(0) \right]. \quad (3.26)$$

We see from (3.26) that $\mathcal{M}_q(\mathbf{y}^s, t_q(\mathbf{y}^s))$ depends on *differential arrival times*, which means that we expect it to have a minimum when

$$\tilde{\tau}_p^{(1)} - \tilde{\tau}_q^{(1)} = t_p(\mathbf{y}^s) - t_q(\mathbf{y}^s).$$

Therefore, this functional can only have good cross-range resolution. It cannot have good range resolution because there is essentially no range information in it. The large conical uncertainty regions to the right of the targets (in red color) in Figures 13 and 14, are produced by the attenuation factor $e^{-\beta|x_p-x_q|^2}$ where the parameter β is adjusted to match the behavior the DOA estimator (3.14).

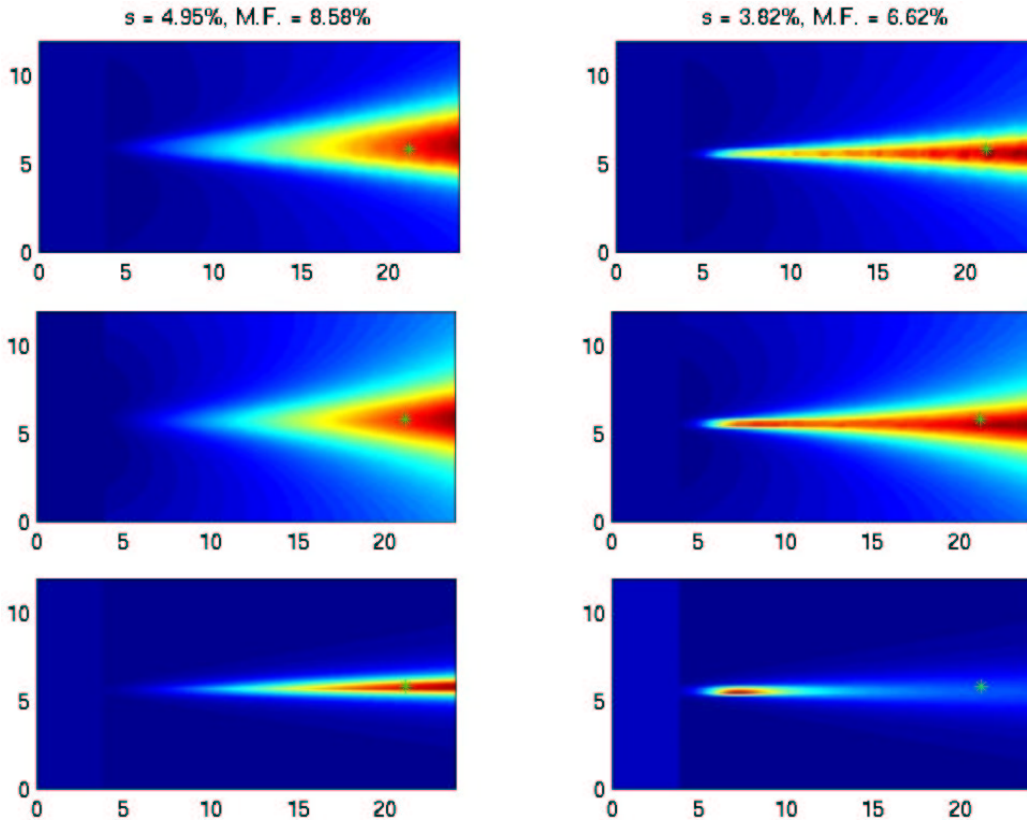


Figure 15: Comparison of direction of arrival (DOA) estimators for simulations with a single target and for two realizations of random media. In the top row we show the functional $\mathcal{R}(\mathbf{y}^s)$ given by (3.14), which requires no arrival time estimation. In the second row we show the direction of arrival estimator given by (3.25), with the β adjusted to match the top row and arrival times estimated from the diagonal of the response matrix. In the third row we show the results of estimating target location with the differential arrival time estimator (3.27).

In Figure 15 we compare results using the simplified model (3.23) with the DOA estimator (3.21), which needs no arrival time estimates. The parameter β in (3.23) is adjusted to reproduce qualitatively the behavior of (3.21) and the arrival times $\tilde{\tau}_p^{(1)}$ are estimated from $P_{pp}(t)$. For the numerical computations we used the two dimensional Green's function in (3.23) (that is replace r_p, r_p^s with $\sqrt{r_p}, \sqrt{r_p^s}$) We see from the two top rows of Figure 15 that the model estimator (3.23) reproduces very well the range uncertainty of the DOA estimator (3.21). For comparison we show in the third row the behavior of the estimator

$$\mathcal{R}_{\Delta-ATA} = \frac{\min_{\mathbf{y}^s} \mathcal{G}_{\Delta-ATA}(\mathbf{y}^s)}{\mathcal{G}_{\Delta-ATA}(\mathbf{y}^s)}, \quad (3.27)$$

which uses only *differential arrival times* when

$$\mathcal{G}_{\Delta-ATA}(\mathbf{y}^s) = \sum_{p,q=1}^N \left[\tilde{\tau}_p^{(1)} - \tilde{\tau}_q^{(1)} - (t_p(\mathbf{y}^s) - t_q(\mathbf{y}^s)) \right]^2. \quad (3.28)$$

We see from the third row of Figure 15 that the differential arrival time estimator (3.28) is not statistically stable like (3.21), shown in the first row. In fact it gives a poor estimate of the target's

position in the bottom right of Figure 15. This is due to the large difference between the estimated random times $\tilde{\tau}_p^{(1)}$, $p = 1, \dots, N$ and the deterministic ones $t_p(\mathbf{y}_1)$, $p = 1, \dots, N$ as shown in Figure 16. This difference may be caused by an unusual realization of the random medium that produces a large error in the estimation of $\tilde{\tau}_p^{(1)}$, $p = 1, \dots, N$. Random arrival times are not easy to estimate in practice, as we explain in Section 3.5.1.

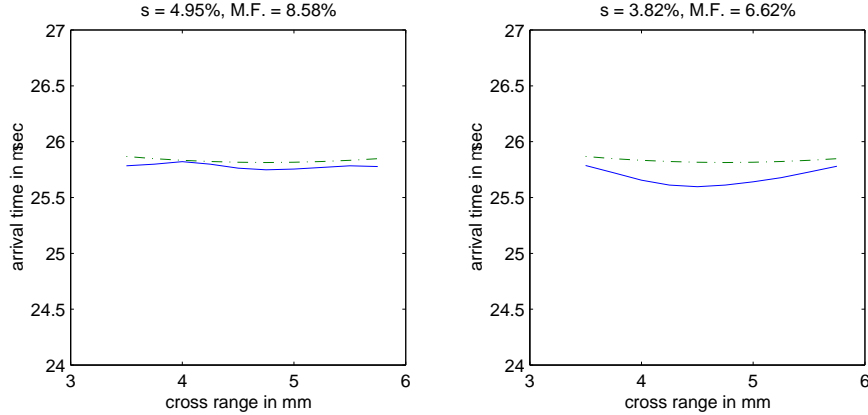


Figure 16: Comparison between the random arrival times $\tilde{\tau}_p$, $p = 1, \dots, N$ (continuous line), estimated from the diagonal of the response matrix and the deterministic arrival times $t_p(\mathbf{y}_1)$, $p = 1, \dots, N$ (dashed line).

To summarize, the time domain DOA estimator (3.21) is statistically stable and gives good cross-range resolution because it uses *implicitly* differential arrival times, with no need to estimate random arrival times as is typical of array processing methods. This is what we infer from the behavior of the model estimator (3.23) where the differential arrival times, which are hidden in the random Green's functions, now appear explicitly. The differential arrival time estimator (3.28) uses only estimated arrival times and is not stable statistically. The DOA estimator (3.21) that requires no arrival time estimation and is statistically stable is clearly superior. But it is sensitive to lack of range information as we see from the large conical regions around the targets, in Figures 13 and 14, bottom left.

3.3.4 DOA estimation with arrival times

We discuss next one way in which arrival time estimates can be used with a DOA estimator. We return to this issue in Section 3.6 after a detailed discussion of arrival time estimation in Sections 3.5.1 and 3.5.2.

The idea is to construct functionals that use both differential and absolute arrival times. We consider only the single target case ($j = 1$) for simplicity. For a search point \mathbf{y}^s we compute

$$\mathcal{H}_q^{(1)}(\mathbf{y}^s) = \mathcal{B}_q^{(1)}(\mathbf{y}^s, \tau_q^{(1)}) - \mathcal{A}_q^{(1)}(\mathbf{y}^s, t_q(\mathbf{y}_s)) \quad (3.29)$$

with

$$\begin{aligned}\mathcal{A}_q^{(1)}(\mathbf{y}^s, t) &= \int_{-\infty}^{\infty} e^{-i\omega t} |\hat{f}(\omega)| |\hat{\xi}_1(\omega)| \hat{G}_0(\mathbf{y}^s, \mathbf{x}_q, \omega) \sum_{p=1}^N \hat{G}(\mathbf{y}_1, \mathbf{x}_p, \omega) \overline{\hat{G}(\mathbf{y}_1, \mathbf{x}_p, \omega)} d\omega, \\ \mathcal{B}_q^{(1)}(\mathbf{y}^s, t) &= \int_{-\infty}^{\infty} e^{-i\omega t} |\hat{f}(\omega)| |\hat{\xi}_1(\omega)| \hat{G}(\mathbf{y}_1, \mathbf{x}_q, \omega) \sum_{p=1}^N \hat{G}_0(\mathbf{y}^s, \mathbf{x}_p, \omega) \overline{\hat{G}(\mathbf{y}_1, \mathbf{x}_p, \omega)} d\omega.\end{aligned}\tag{3.30}$$

Here $\tau_p^{(1)}$, $p = 1, \dots, N$ are arrival times estimated from the effective singular vectors (see Section 3.5.2), which are much better than the estimates $\tilde{\tau}_p^{(1)}$, $p = 1, \dots, N$ obtained from the diagonal of the response matrix. We then construct the Direction-of-Arrival Arrival-Time (DOA-AT) estimator

$$\mathcal{G}_\tau^{(1)}(\mathbf{y}^s) = \sum_{p=1}^N \left(\mathcal{H}_p^{(1)}(\mathbf{y}^s) \right)^2,\tag{3.31}$$

and display

$$\mathcal{R}_\tau(\mathbf{y}^s) = \frac{\min_{\mathbf{y}^s} \mathcal{G}_\tau^{(1)}(\mathbf{y}^s)}{\mathcal{G}_\tau^{(1)}(\mathbf{y}^s)}.\tag{3.32}$$

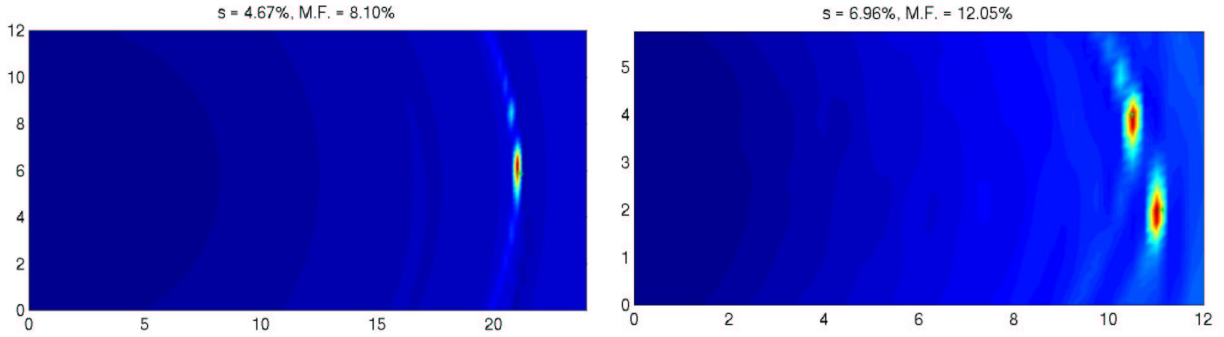


Figure 17: Estimates of one target and two targets in a random medium using the DOA-AT estimator (3.32). The range uncertainty of the DOA estimator (3.14), seen in Figures 13 and 14, is eliminated.

Simulation results using the DOA-AT estimator (3.32), for one and two targets, are shown in Figure 17. Clearly the functional (3.31) gives a good estimate of both the range and the cross-range of the targets. However, it is sensitive to the quality of the arrival time estimates $\tau_p^{(1)}$, $p = 1, \dots, N$. In Section 3.6 we introduce an alternative functional which is more efficient and robust : it gives a better estimate of the locations of the targets and is less sensitive to arrival time estimates.

It is clear from the analysis of this section that methods not using arrival time estimation but providing range information are important. One such widely used method is Synthetic Aperture Imaging (SAI) which we discuss in the next section.

3.4 Synthetic Aperture Imaging (SAI)

In Synthetic Aperture Imaging (Cheney, 2001) we measure only the diagonal $P_{pp}(t)$ of the response matrix and we locate point scatterers using deterministic travel times. At a search point \mathbf{y}^s in the

domain of interest we compute the deterministic arrival time for $P_{pp}(t)$. That is, the time to go from the p^{th} transducer to the search point \mathbf{y}^s and then come back to the p^{th} transducer. This is twice the arrival time $t_p(\mathbf{y}^s)$ given by (3.12). The target locations are estimated as the maxima of the absolute value of the objective function

$$\mathcal{R}(\mathbf{y}^s) = \sum_{p=1}^N P_{pp}(2t_p(\mathbf{y}^s)). \quad (3.33)$$

For large synthetic arrays with transducers that have a limited angular aperture, which is the usual case, we should not sum over all transducer locations \mathbf{x}_p , $p = 1, \dots, N$, but only over the ones that illuminate the region of interest at some range L , as shown in Figure 18.

Synthetic aperture imaging with (3.33) is an arrival time imaging method, as we now explain in the single target case. Let us suppose that there is only one target located at \mathbf{y}_1 . In the frequency

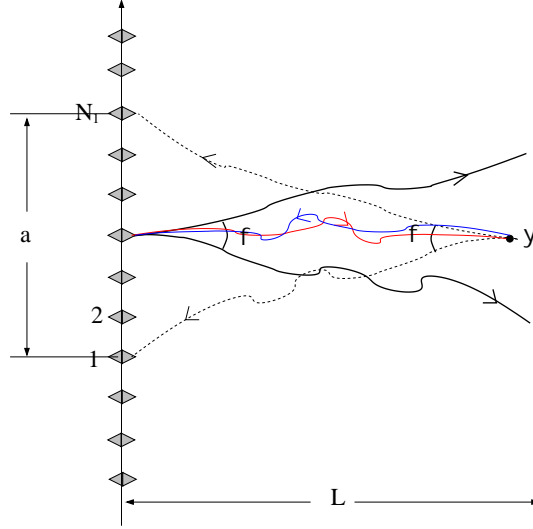


Figure 18: Synthetic aperture imaging (SAI). The array is very large so to image a particular region we use only the part of the array that illuminates it.

domain the SAI measurements are modeled by

$$\widehat{P}_{pp}(\omega) = \widehat{f}(\omega)\widehat{\xi}_1(\omega)\widehat{Q}_{pp}(\omega), \quad (3.34)$$

where

$$\widehat{Q}_{pp}(\omega) = \widehat{G}^2(\mathbf{x}_p, \mathbf{y}_1, \omega). \quad (3.35)$$

In a homogeneous medium the three-dimensional Green's function is given by

$$G_0(\mathbf{x}_p, \mathbf{y}_1, \omega) = \frac{e^{ik|\mathbf{x}_p - \mathbf{y}_1|}}{4\pi |\mathbf{x}_p - \mathbf{y}_1|} \quad (3.36)$$

and so, in the time domain,

$$Q_{pp}(t) = \frac{1}{16\pi^2 |\mathbf{x}_p - \mathbf{y}_1|^2} \int_{-\infty}^{\infty} e^{i\omega(2t_p(\mathbf{y}_1) - t)} d\omega = \frac{1}{8\pi |\mathbf{x}_p - \mathbf{y}_1|^2} \delta(t - 2t_p(\mathbf{y}_1)), \quad (3.37)$$

where $\delta(\cdot)$ is the one-dimensional delta function. The objective function (3.33) is then given by

$$\mathcal{R}(\mathbf{y}^s) = \sum_{p=1}^N \frac{1}{8\pi |\mathbf{x}_p - \mathbf{y}_1|^2} \xi_1(t) \star f(2(t_p(\mathbf{y}^s) - t_p(\mathbf{y}_1))), \quad (3.38)$$

where \star stands for convolution in time. For multiple targets we simply sum over them in (3.38)

$$\mathcal{R}(\mathbf{y}^s) \approx \sum_{j=1}^M \sum_{p=1}^N \frac{1}{8\pi |\mathbf{x}_p - \mathbf{y}_j|^2} \xi_j(t) \star f(t_p(\mathbf{y}^s) - t_p(\mathbf{y}_j)), \quad (3.39)$$

neglecting multiple scattering between the targets.

Given the small support of the pulse $f(t)$, appropriate for a broad-band probing signal, $\mathcal{R}(\mathbf{y}^s)$ peaks at search points \mathbf{y}^s with arrival time $t_p(\mathbf{y}^s) \approx t_p(\mathbf{y}_j)$. The SAI functional (3.39) shows clearly the role of the probing pulse on the resolution of the images. The shorter the pulse $f(t)$, the better the *range* resolution in (3.39). Cross-range resolution is, in principle, very good for large SAI in a homogeneous medium (Cheney, 2001).

In random media, however, the arrival times of the scattered echos differ from $t_p(\mathbf{y}_j)$, so we expect that the quality of the images degrades when the random sound speed fluctuations increase. Moreover, the objective function (3.33) is not statistically stable, and images can vary significantly from one realization of the randomly inhomogeneous medium to another. That is because in (3.33) the square of the random Green's function $\widehat{G}^2(\mathbf{x}_p, \mathbf{y}_1, \omega)$ appears. It carries a large random phase because there is no complex conjugation (time reversal) in (3.33) to eliminate it, as in the DOA estimation in Section 3.3. Only functionals in which such large phases cancel can be self-averaging, and therefore useful for imaging in random media. Range resolution, however, is controlled mainly by the bandwidth of the probing pulse while summing over transducer locations smooths out fluctuations and gives acceptable results.

In Figures 19 and 20 we plot the absolute value of the objective function (3.33) as a function of range and cross-range of the search point \mathbf{y}^s . In random media the estimates of the target locations are quite unsatisfactory, especially the cross-range, for simulations with both one target (Figure 19) and two targets (Figure 20). The statistical instability is also seen clearly.

3.5 Arrival time analysis

As we have seen in Sections 3.3.2 and 3.3.3, direction of arrival estimates do not provide information about the range of the targets. We get this from the arrival times and amplitudes of the recorded back-scattered echos.

3.5.1 Arrival time estimation and imaging

For a single target, an easy way to estimate arrival times from the unknown target to the array is to use the diagonal of the response matrix as in SAI. The arrival time in $P_{pp}(t)$ is twice the arrival time from the unknown target to the p^{th} transducer. For multiple targets the time traces of the diagonal of the response matrix $P_{pp}(t)$ contain scattered fronts from all the targets and they are difficult to interpret, especially when the medium is randomly inhomogeneous as we see in Figure 21. Here the traces of $P_{pp}(t)$ are from numerical simulations with two targets embedded in a homogeneous medium and a random medium with standard deviation $s = 6.68\%$. It is clearly difficult to estimate arrival times for the second front in the random medium.

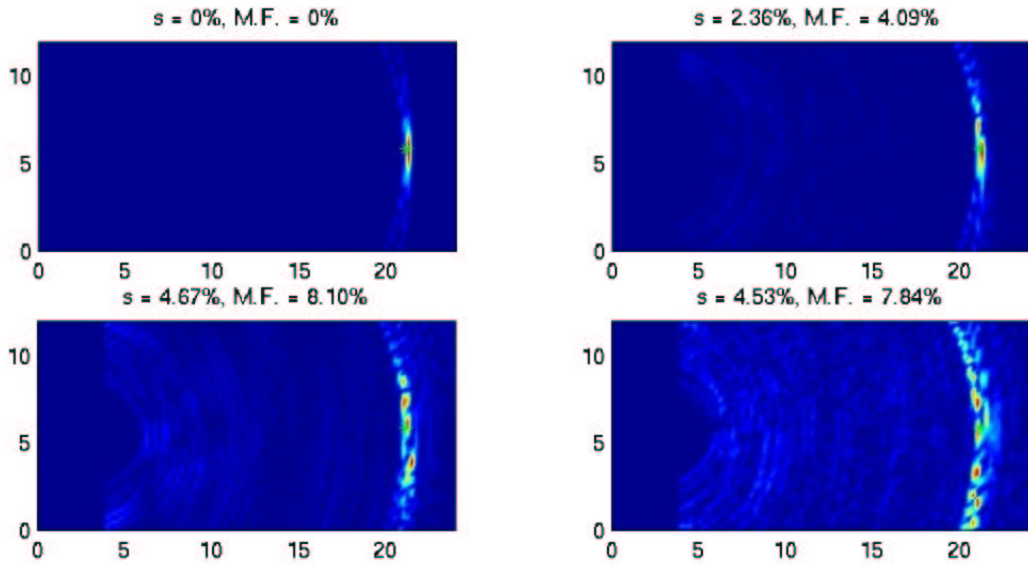


Figure 19: The SAI estimate of the location of one target in random media with different strength of the fluctuations of the sound speed. The exact location of the target is denoted by the green star. The standard deviation s and maximum fluctuations (M.F.) are indicated on the top of each view. The horizontal axis is the range in mm and the vertical axis is the cross-range in mm.

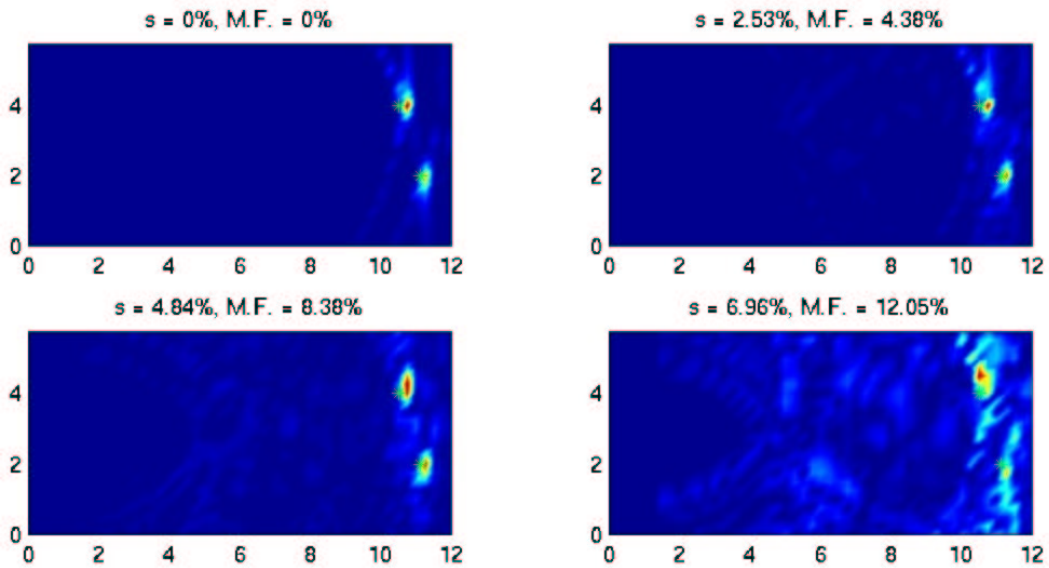


Figure 20: Similar to Figure 19 but with two targets.

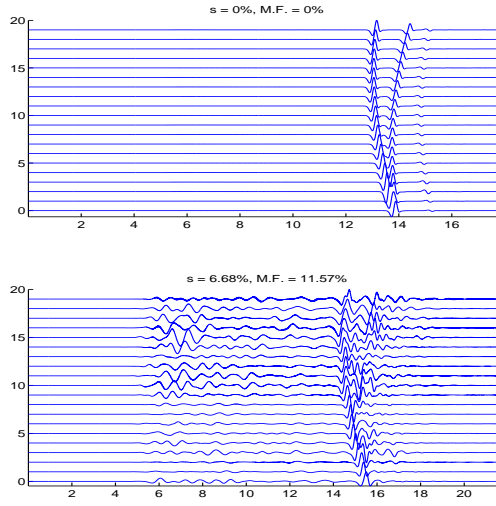


Figure 21: Traces of the diagonal part of the response matrix $P_{pp}(t)$ for a homogeneous medium and a random medium with standard deviation $s = 6.68\%$ and maximum fluctuation M.F. = 11.57% . The horizontal axis is time, in microseconds.

If we have reasonable estimates of arrival times from the diagonal of the response matrix we can try to image the targets using only these estimates with the following objective functional. Let $\tilde{\tau}_p^{(j)}$ be the estimated arrival times for the scattered fronts $j = 1, \dots, M$ ($M = 2$ in Figure 21) and transducers $p = 1, \dots, N$ ($N = 20$ in Figure 21). For a search point \mathbf{y}^s we compute the deterministic arrival times $t_p(\mathbf{y}^s)$ from (3.12) and we define the Arrival Time Analysis (ATA) estimator functional

$$\mathcal{R}_{ATA}(\mathbf{y}^s) = \sum_{j=1}^M \frac{\min_{\mathbf{y}^s} \mathcal{G}_{ATA}^{(j)}(\mathbf{y}^s)}{\mathcal{G}_{ATA}^{(j)}(\mathbf{y}^s)}, \quad (3.40)$$

where

$$\mathcal{G}_{ATA}^{(j)}(\mathbf{y}^s) = \sum_{p=1}^N \left[\tilde{\tau}_p^{(j)} - 2t_p(\mathbf{y}^s) \right]^2. \quad (3.41)$$

The estimates of the target locations are the maxima of functional $\mathcal{R}(\mathbf{y}^s)$, which we show in Figure 22 in the left column. In random media we can get good estimates of the arrival times $\tilde{\tau}_p^{(1)}$ from the first front but rather poor estimates of the arrival times $\tilde{\tau}_p^{(2)}$ from the second front. This is seen in Figure 22 (left column) where the image of the second target is not so good.

It is interesting to combine the ATA estimator (3.40) with the Δ -ATA estimator (3.27) that uses only differential arrival times and has good cross-range resolution. By combining we mean that we take as estimator the sum of the products

$$\mathcal{G}_C = \sum_{j=1}^M \mathcal{G}_{ATA}^{(j)}(\mathbf{y}^s) \cdot \mathcal{G}_{\Delta-ATA}^{(j)}(\mathbf{y}^s) \quad (3.42)$$

with $\mathcal{G}_{ATA}^{(j)}(\mathbf{y}^s)$ given by (3.41) and $\mathcal{G}_{\Delta-ATA}^{(j)}(\mathbf{y}^s)$ given by (3.28), in the one-target case. Simulation results are shown in Figure 22, right column. Cross range resolution is somewhat better when differential arrival times are used, as expected.

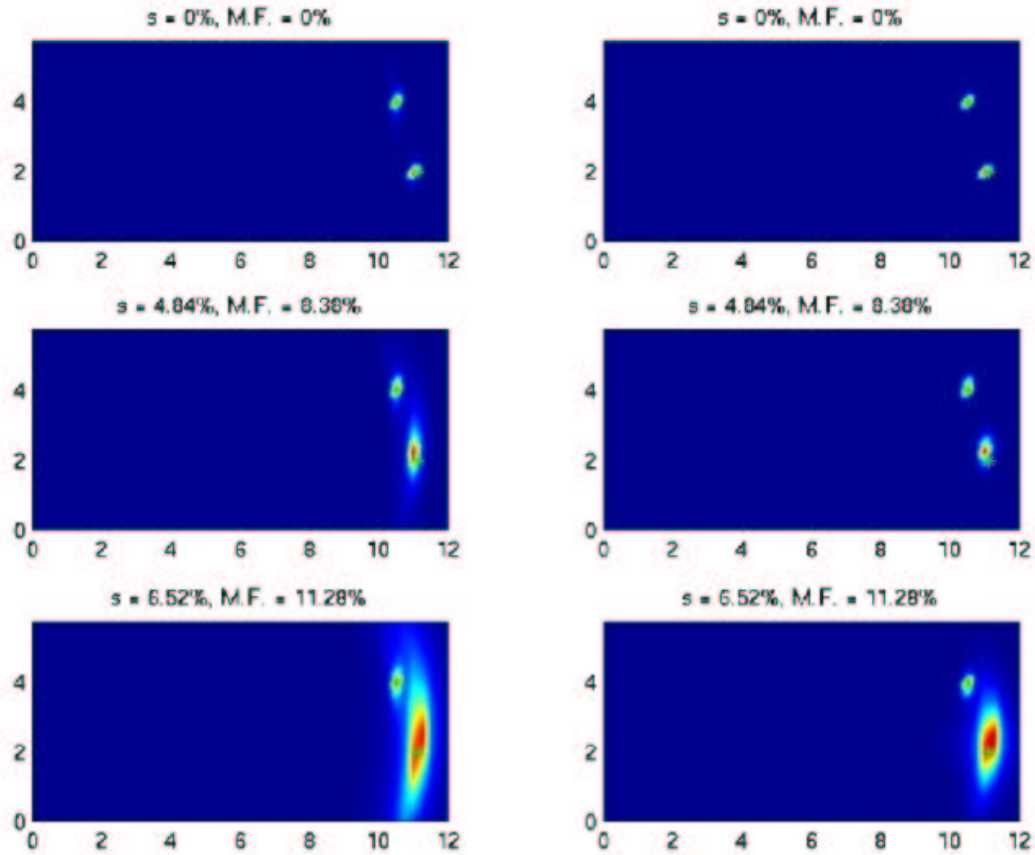


Figure 22: The ATA estimate (3.40) (left column) and the estimate obtained by combining ATA with Δ -ATA (3.27) (right column) of two target in random media with different strength of the fluctuations of the sound speed. The exact location of the targets are denoted by the green stars. The standard deviation s and maximum fluctuations (M.F.) are indicated on the top of each view. The horizontal axis is the range in mm and the vertical axis is the cross-range in mm.

3.5.2 Arrival time estimation using the SVD

We can improve our estimates of arrival times considerably by using the singular vectors of the response matrix. These vectors have already been used in direction of arrival estimation, as explained in Section 3.3. We use them now to illuminate each target separately, while shading the others, so that arrival times of scattered fronts can be estimated more accurately than when using only the diagonal of the response matrix as in SAI.

When the targets are sufficiently far apart, or have sufficiently different strengths, the singular values $\sigma_j(\omega), j = 1, \dots, M$, of the response matrix $\hat{P}(\omega)$ are well-separated over the frequency band of the pulse $f(t)$. The traces of the singular vectors $\mathbf{U}_j(t)$ have only one coherent front (one arrival time) back-scattered by the target that makes the largest contribution to the singular value $\sigma_j(\omega), j = 1, \dots, M$. This does not mean that we require $\hat{\mathbf{g}}^H(\mathbf{y}_j, \omega)\hat{\mathbf{g}}(\mathbf{y}_h, \omega) \approx 0$ for $j \neq h$ or, equivalently, that the targets are so far apart that they are essentially isolated from each other. It does mean, however, that the contribution of the illuminating Green's vector $\hat{\mathbf{g}}(\mathbf{y}_j, \omega)$ in $\hat{\mathbf{U}}_j(\omega)$ is more significant than that of the vectors $\hat{\mathbf{g}}(\mathbf{y}_h, \omega)$, for $h \neq j$.

Let us suppose that the target at \mathbf{y}_1 is the strongest with $\sigma_1(\omega)$ separated from all other singular values over the frequency band of $\hat{P}(\omega)$. The singular vector $\hat{\mathbf{U}}_1(\omega)$ of $\hat{P}(\omega)$ is normalized ($\|\hat{\mathbf{U}}_1(\omega)\| = 1$) but carries an arbitrary, frequency dependent, phase. Because of this $\mathbf{U}_1(t)$ looks incoherent in the time domain. We can, however, calculate N , coherent in time, versions of the leading singular vector by projecting the columns of the response matrix onto it

$$\hat{\mathbf{U}}_1^{(p)}(\omega) = \left[\hat{\mathbf{U}}_1(\omega)^H \hat{\mathbf{P}}^{(p)}(\omega) \right] \hat{\mathbf{U}}_1(\omega), \quad p = 1, \dots, N. \quad (3.43)$$

Here $\hat{\mathbf{P}}^{(p)}$ is the p^{th} column of the response matrix $\hat{P}(\omega)$. Clearly $\hat{\mathbf{U}}_1^{(p)}(\omega)$ is a singular vector of $\hat{P}(\omega)$ and it carries the phase of its p^{th} column, so that in the time domain $\mathbf{U}_1^{(p)}(t)$ is coherent and arrival times can be estimated. The singular vector $\hat{\mathbf{U}}_1^{(p)}(t)$ can be obtained by iterated time reversal and back propagation as was done in (Prada et al., 1996).

For a single target

$$\hat{\mathbf{U}}_1^{(p)}(\omega) = \hat{f}(\omega)\hat{\xi}_1(\omega)\hat{G}(\omega, \mathbf{x}_p, \mathbf{y}_1)\hat{\mathbf{g}}(\omega, \mathbf{y}_1). \quad (3.44)$$

For multiple targets $\hat{\mathbf{U}}_1^{(p)}(\omega)$ is more complicated and contains contributions from the other targets. But when the target located at \mathbf{y}_1 is the strongest and its presence is dominant in the time trace of the singular vector, for the estimation of arrival times we can still consider the one-target expression (3.44) as valid approximately.

The various versions of the leading singular vector calculated by (3.43) have different arrival times because of the phase differences introduced by the Green's function $\hat{G}(\omega, \mathbf{x}_p, \mathbf{y}_1)$. However, we can synchronize them and then average them (stack them) to obtain the effective singular vector

$$\langle \mathbf{U}_1(t) \rangle = \frac{1}{N} \sum_{p=1}^N \mathbf{U}_1^{(p)}(t - \tau_p^{(1)}). \quad (3.45)$$

The synchronization of $\mathbf{U}_1^{(p)}(t)$ requires the estimates of travel times $\tau_p^{(1)}$, from emitting transducer p to target location \mathbf{y}_1 . These times are estimated as the minimizers of

$$\min_{\tau_p^{(1)}} \int_0^T \sum_{p=1}^N \left[\mathbf{U}_1^{(p)}(t - \tau_p^{(1)}) - \frac{1}{N} \sum_{q=1}^N \mathbf{U}_1^{(q)}(t - \tau_q^{(1)}) \right]^2 dt, \quad (3.46)$$

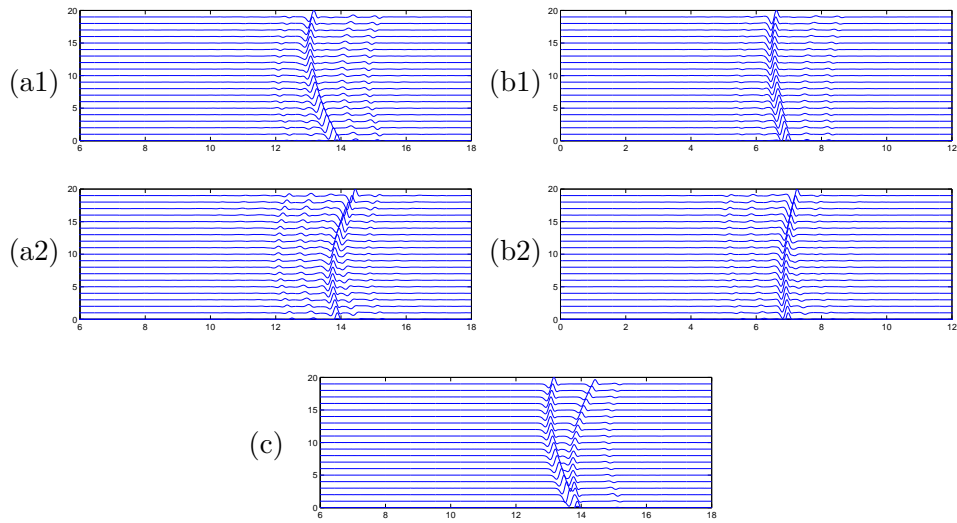


Figure 23: Traces computed from the diagonal of the singular vector matrix for the homogeneous medium. In figures (a1) and (a2) we show the traces from the diagonal of the first and the second singular vector matrix. In figures (b1) and (b2) we show the traces of the first and second averaged singular vector. In figure (c) we show the traces from the diagonal of the response matrix. There is no averaging in (a1), (a2) and (c).

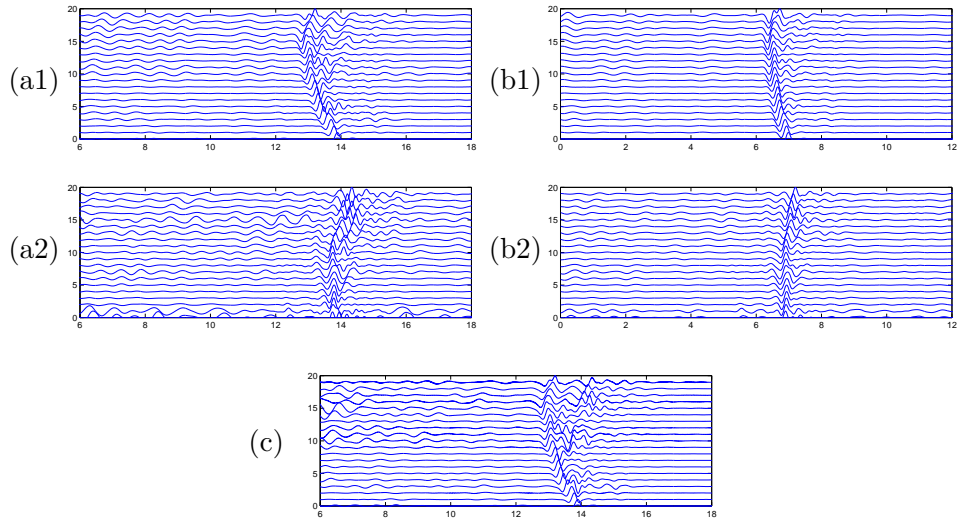


Figure 24: Same as in Figure 23 but for the random medium with $s = 6.68\%$

for some time T large enough to capture the scattered echos in $\mathbf{U}_1^{(p)}(t)$, for $p = 1, \dots, N$.

The time trace of $\langle \mathbf{U}_1(t) \rangle$ is cleaner than any individual trace because of the averaging. But we are more interested in the estimates of the arrival times $\tau_p^{(1)}$ that come out of (3.46) and we now show how they can be used. Arrival time estimates for other targets are obtained in the same way, by starting with the second singular vector of the response matrix, etc.

3.6 Subspace arrival time analysis (SAT)

We are now ready to introduce an imaging method that combines the direction of arrival analysis (see Section 3.3) with the arrival time analysis (see Section 3.5.2).

For each search point \mathbf{y}^s we compute the objective functional

$$\mathcal{R}_{SAT}(\mathbf{y}^s) = \sum_{j=1}^M \frac{\min_{\mathbf{y}^s} \mathcal{G}_{SAT}^{(j)}(\mathbf{y}^s)}{\mathcal{G}_{SAT}^{(j)}(\mathbf{y}^s)}, \quad (3.47)$$

where

$$\mathcal{G}_{SAT}^{(j)}(\mathbf{y}^s) = \sum_{p=1}^N \left[\mathcal{F}_p^{(j)}(\mathbf{y}^s, t_p(\mathbf{y}^s)) \right]^2 \left[\tau_p^{(j)} - t_p(\mathbf{y}^s) \right]^2. \quad (3.48)$$

Here $\mathcal{F}^{(j)}(\mathbf{y}^s, t)$ is defined by (3.11), $t_p(\mathbf{y}^s)$, $p = 1, \dots, N$ are the deterministic arrival times given by (3.12) and $\tau_p^{(j)}$, $p = 1, \dots, N$, $j = 1, \dots, M$ are the arrival times computed in (3.46). We call (3.47) the Subspace Arrival Time (SAT) estimator. In Figures 25 and 26 we show the results of simulations using this estimator. As we can see from the results this imaging method is very

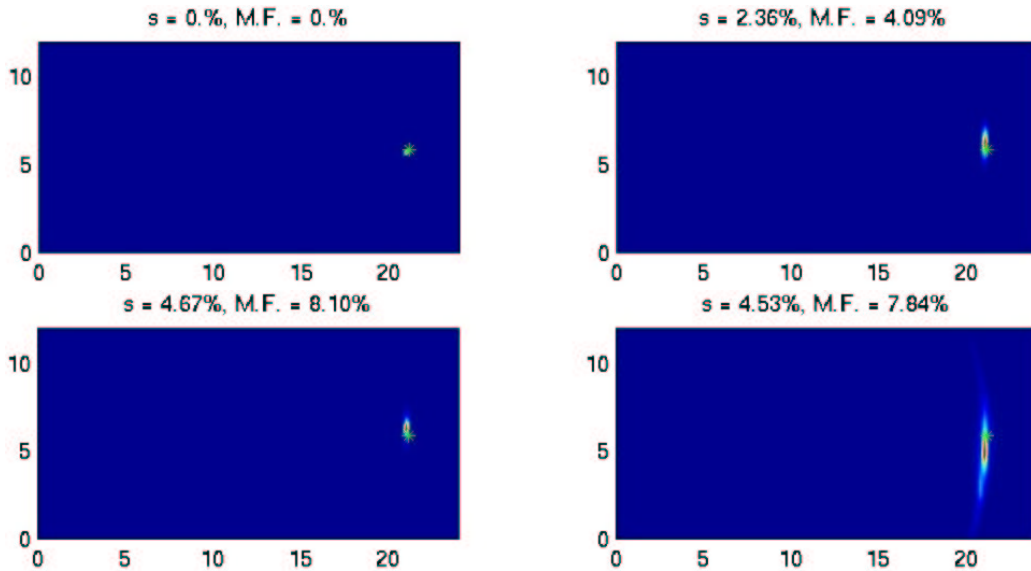


Figure 25: The SAT estimate of one target in random media with different strength of the fluctuations of the sound speed. The exact location of the target is denoted by the green star. The standard deviation s and maximum fluctuations (M.F.) are indicated on the top of each view. The horizontal axis is the range in mm and the vertical axis is the cross-range in mm.

robust. The target locations are estimated well even in the case of random media with strong

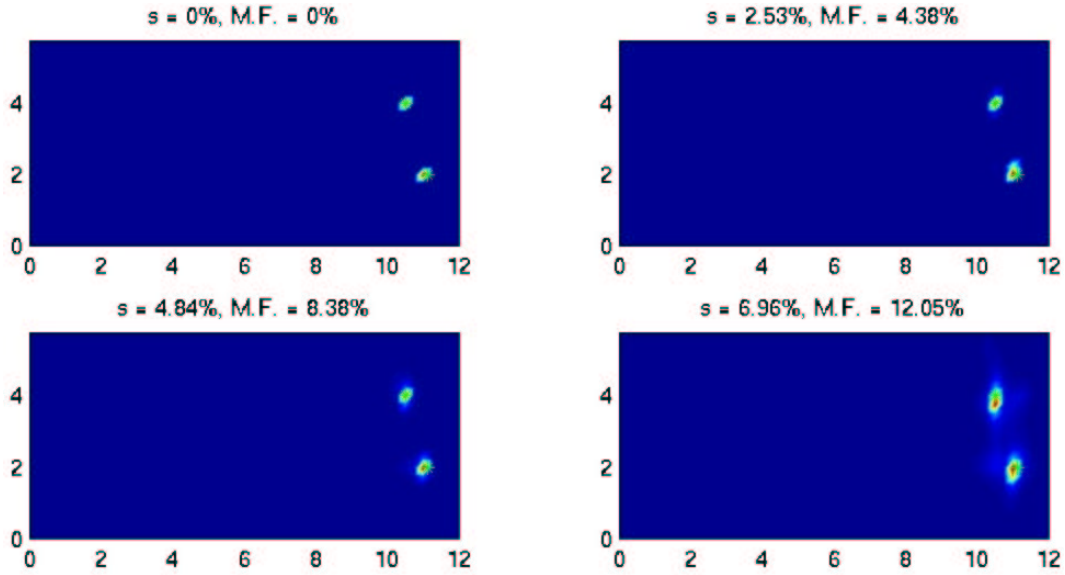


Figure 26: The SAT estimate as in Figure 25 for two targets.

inhomogeneities (maximum fluctuations in the velocity up to 12%). Another important property of SAT is statistical stability. Target location estimates do not change for different realizations of the random media. The functional (3.47) is more robust than the functional (3.29) discussed in Section 3.3.3. This is because the probing pulse is very short (broad-band signal), so evaluating the first term $\mathcal{B}_q^{(1)}(\mathbf{y}^s, t)$ at time $t = \tau_q^{(1)}$ makes the functional (3.29) sensitive to errors in the estimates of arrival times.

The basic limitation of SAT imaging (3.47) comes from the assumption that each singular vector of the matrix $\hat{P}(\omega)$ can be associated with one target. What is actually important here is that the ordering of the singular values does not change with frequency, over the bandwidth of $\hat{f}(\omega)$. If the singular values cross as frequency varies, then we need to track this crossing. For example, by identifying the singular values from the form of the corresponding singular vectors instead of using their relative amplitude.

SAT imaging works well because it combines good estimation of both direction of arrival, DOA, and arrival times, ATA. In Sections 3.3.3 and 3.4 we discussed sensitivity of DOA to arrival time, and hence range estimation. We discussed in Section 3.3.4 the possibility of using estimators that do not use direct arrival time estimation at all, like the DOA estimator (3.14) and the SAI estimator (3.33). We can combine these two estimators much as we did with ATA and Δ -ATA in (3.42). A no-explicit arrival time estimator, DOA-SAI, is

$$\mathcal{R}_{\text{DOA-SAI}}(\mathbf{y}^s) = \sum_{j=1}^M \frac{\mathcal{G}_{\text{DOA-SAI}}^{(j)}(\mathbf{y}^s)}{\max_{\mathbf{y}^s} \mathcal{G}_{\text{DOA-SAI}}^{(j)}(\mathbf{y}^s)} \quad (3.49)$$

where

$$\mathcal{G}_{\text{DOA-SAI}}^{(j)}(\mathbf{y}^s) = \left| \sum_{p=1}^N P_{pp}(2t_p(\mathbf{y}^s)) \right| / \mathcal{G}^{(j)}(\mathbf{y}^s) \quad (3.50)$$

and with $\mathcal{G}^{(j)}(\mathbf{y}^s)$ given by (3.13).

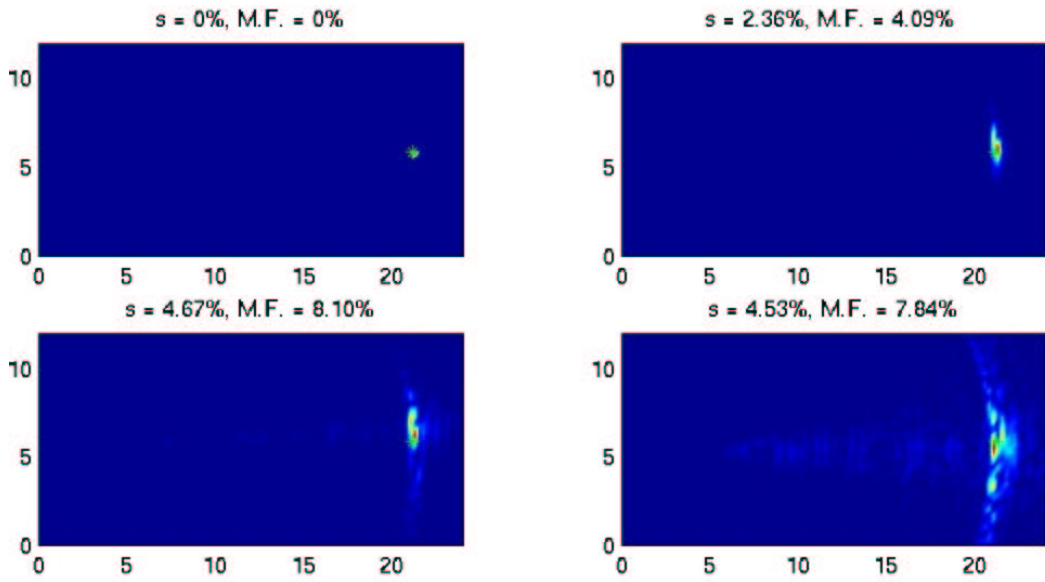


Figure 27: Combined DOA (3.13) and SAI (3.33) estimation of one target location in random media with different strength of the fluctuations of the sound speed. The exact location of the target is denoted by the green star. The standard deviation s and maximum fluctuations (M.F.) are indicated on the top of each view. The horizontal axis is the range in mm and the vertical axis is the cross-range in mm.

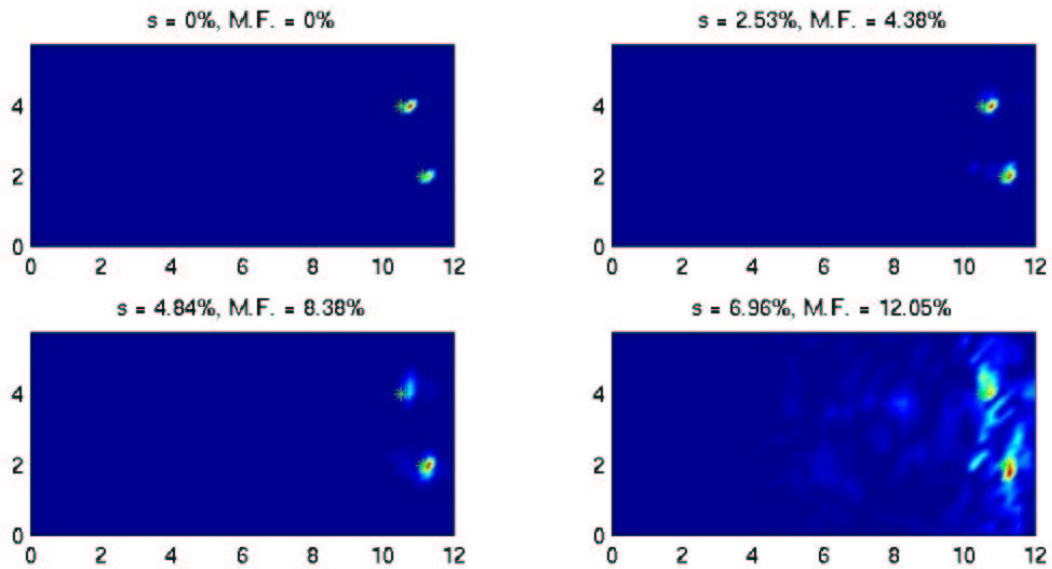


Figure 28: Same as Figure 27 with two targets.

In Figures 27 and 28 we show one and two target simulation results using (3.49). It is not as good as SAT (Figures 25 and 26) but it is better than DOA (Figures 13 and 14) and SAI (Figures 19 and 20). This is as expected, of course, but it is interesting to see how range and cross-range estimation interact and influence each other in a random medium.

4 Summary and conclusions

For each frequency we record an $N \times N$ array response matrix $\hat{P}(\omega)$. In an ideal situation this matrix is a complex linear combination of M rank one complex symmetric matrices, each of which corresponds to one of the M targets in the medium. For $N > M$ one can determine the number of targets by calculating the number of non-zero singular values of $\hat{P}(\omega)$. If the targets are well separated, linear matched filter techniques can be used to determine their locations. In practice we need to consider the effect of inhomogeneities in the ambient medium and this is what we do in this paper.

Active array probing of small scatterers in random media poses special problems that require a careful assessment of imaging methodology. Based on our understanding of time reversal in random media (Blomgren et al., 2002), super-resolution and its statistical stability in the time domain in particular, we have identified a number of imaging methods that give good estimates for the location of the scatterers. The key idea is to use a subspace projection method in the time domain that is statistically stable (Section 3.3). We explain carefully the sensitivity of this estimator to range information, in Section 3.3.3, which is somewhat unexpected since in homogeneous media range and cross-range estimation are essentially distinct processes. We explain briefly the well-known inadequacy of synthetic aperture imaging in random media, in Section 3.4. In Section 3.6 we formulate the Subspace Arrival Time (SAT) method that is robust and accurate if we have good arrival time estimates, as we can often get using subspace analysis in the manner of Section 3.5.2.

We have conducted extensive numerical simulations to understand better and to substantiate our theoretical insights into imaging in random media. We are currently working on a more detailed analysis of the quality of various types of array imaging.

Acknowledgments

The work of L. Borcea was partially supported by the National Science Foundation under grant number DMS-9971209 and by DOE DE-FG03-00ER25424. The work of G. Papanicolaou was supported by grants AFOSR F49620-01-1-0465, NSF DMS-9971972, and DOE DE-FG03-00ER25424. The work of J. Berryman performed under the auspices of the U.S. Department of Energy by the University of California Lawrence Livermore National Laboratory under contract No. W-7405-ENG-48 and supported specifically by the LLNL Laboratory Directed Research and Development Program and Environmental Management Sciences Program.

A Multiple scattering between targets

In this appendix we calculate the form of the response matrix when multiple scattering between targets is taken into consideration. Suppose that the M targets are located at $\mathbf{y}_1, \dots, \mathbf{y}_M$. At frequency ω , the response matrix $\hat{P}(\omega) = \left(\hat{P}_{pq}(\omega) \right)$ is given by

$$\hat{P}_{pq}(\omega) = \hat{f}(\omega) \sum_{l=1}^M \sum_{j=1}^M \hat{c}_{jl}(\omega) \hat{G}(\mathbf{y}_j, \mathbf{x}_p, \omega) \hat{G}(\mathbf{y}_l, \mathbf{x}_q, \omega), \quad p, q = 1, \dots, N, \quad (\text{A.1})$$

where $\hat{f}(\omega)$ is the Fourier transform of the probing pulse, \hat{G} is the Green's function for the Helmholtz equation (2.3) in the **random medium** and $\hat{c}_{jl}(\omega)$ are the entries of a complex symmetric matrix

\widehat{C} ($\widehat{C} = \widehat{C}^T$) that we will describe in this appendix. Thus, the response matrix can be written as

$$\widehat{P}(\omega) = \widehat{f}(\omega) \sum_{j=1}^M \sum_{l=1}^M \widehat{c}_{jl}(\omega) \widehat{\mathbf{g}}(\mathbf{y}_j, \omega) \widehat{\mathbf{g}}^T(\mathbf{y}_l, \omega), \quad (\text{A.2})$$

where T denotes transpose and where $\widehat{\mathbf{g}}(\mathbf{y}_j, \omega)$ is the illuminating Green's vector onto the array from the point \mathbf{y}_j , given by (3.3).

If the scatterers are far apart then \widehat{C} is approximately diagonal and we have the response matrix model without multiple scattering between targets that is used in this paper. Multiple scattering of waves with the medium inhomogeneities is, however, fully taken into consideration because the Green's functions are random. That is, they are solutions of the stochastic wave equation. To carry out the imaging of the scatterer locations we do a singular value decomposition and an arrival time analysis as explained in the paper. vector independent

The general model that allows for multiple scattering between the scatterers is obtained in the following way. Suppose that we illuminate from a source point \mathbf{x}_s the cluster of targets $\mathbf{y}_1, \dots, \mathbf{y}_M$ and we record the field at the observation point \mathbf{x}_o as shown in Figure (29).

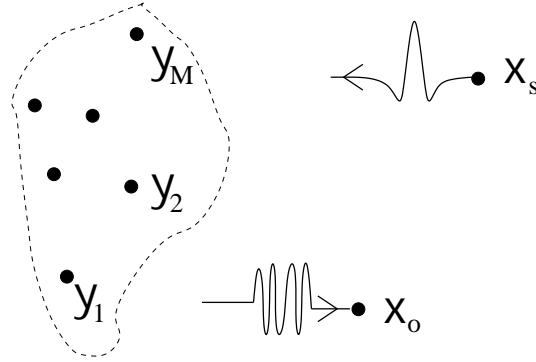


Figure 29: From the source point \mathbf{x}_s we send a pulse $\widehat{f}(\omega)$ that illuminates the cluster of targets $\mathbf{y}_1, \dots, \mathbf{y}_M$. The field, direct and scattered, is recorded at observation point \mathbf{x}_o .

Let $\widehat{G}_d(\mathbf{x}, \mathbf{y})$ be the Green's function between the points \mathbf{x} and \mathbf{y} when there are no scatterers in the randomly inhomogeneous, background medium. Then the Green's function between \mathbf{x}_s and \mathbf{x}_o can be written as,

$$\widehat{G}(\mathbf{x}_o, \mathbf{x}_s) = \widehat{G}_d(\mathbf{x}_o, \mathbf{x}_s) + \sum_{j=1}^M \widehat{G}_d(\mathbf{x}_o, \mathbf{y}_j) \widehat{\xi}_j(\omega) \widehat{F}(\mathbf{y}_j, \mathbf{x}_s), \quad (\text{A.3})$$

with $\widehat{F}(\mathbf{y}_k, \mathbf{x}_s)$ the total field incident upon \mathbf{y}_k ,

$$\widehat{F}(\mathbf{y}_k, \mathbf{x}_s) = \widehat{G}_d(\mathbf{y}_k, \mathbf{x}_s) + \sum_{\substack{j=1 \\ j \neq k}}^M \widehat{G}_d(\mathbf{y}_k, \mathbf{y}_j) \widehat{\xi}_j(\omega) \widehat{F}(\mathbf{y}_j, \mathbf{x}_s). \quad (\text{A.4})$$

We see that $\widehat{F}(\mathbf{y}_j, \mathbf{x}_s)$ can be determined by solving the linear system,

$$\sum_{k=1}^M \Gamma_{jk} \sqrt{\widehat{\xi}_k(\omega)} \widehat{F}(\mathbf{y}_k, \mathbf{x}_s) = \sqrt{\widehat{\xi}_j(\omega)} \widehat{G}_d(\mathbf{y}_j, \mathbf{x}_s), \quad (\text{A.5})$$

with

$$\Gamma_{jk} = \delta_{jk} - \sqrt{\widehat{\xi}_j(\omega)}\sqrt{\widehat{\xi}_k(\omega)}(1 - \delta_{jk})\widehat{G}_d(\mathbf{y}_k, \mathbf{y}_j), \quad (\text{A.6})$$

which is a complex symmetric matrix.

The matrix $\widehat{C} = (\widehat{c}_{jl})$ in (A.1) or (A.2) is then given by

$$\widehat{c}_{jl}(\omega) = \sqrt{\widehat{\xi}_j(\omega)}\sqrt{\widehat{\xi}_l(\omega)}(\Gamma^{-1})_{jl} \quad (\text{A.7})$$

where we assume that the matrix Γ is invertible. This will be the case when the scatterers are not too close to each other or the scattering amplitudes $\widehat{\xi}_j$ are small. If the scatterers are far apart then Γ is close to the identity and \widehat{C} is diagonal with entries ξ_j . Multiple scattering between targets is negligible in this case. If they are clustered close to each other then the Green's function \widehat{G}_d in (A.6) can be taken to be the deterministic one, \widehat{G}_0 , since the effect of random inhomogeneities over short distances is negligible. For clusters of scatterers the matrix \widehat{C} is therefore deterministic. The detailed analysis of imaging several distinct clusters of targets will be presented elsewhere.

References

- Bécache, E., Joly, P., and Tsogka, C. (1997). Etude d'un nouvel élément fini mixte permettant la condensation de masse. *C. R. Acad. Sci. Paris Sér. I Math.*, 324:1281–1286.
- Bécache, E., Joly, P., and Tsogka, C. (2000). An analysis of new mixed finite elements for the approximation of wave propagation problems. *SIAM J. Numer. Anal.*, 37:1053–1084.
- Bérenger, J. (1994). A perfectly matched layer for the absorption of electromagnetic waves. *J. Comput. Phys.*, 114:185–200.
- Bleistein, N., Cohen, J., and Jr., J. S. (2001). *Mathematics of multidimensional seismic imaging, migration, and inversion*. Springer, New York.
- Blomgren, P., Papanicolaou, G., and Zhao, H. (2002). Super-resolution in time-reversal acoustics. *J. Acoust. Soc. Am.*, 111:238–248.
- Born, M. and Wolf, E. (1970). *Principles of Optics*. Academic Press, New York.
- Cheney, M. (2001). A mathematical tutorial on synthetic aperture radar. *SIAM Review*, 43:301–312.
- Claerbout, J. F. (1985). *Fundamentals of geophysical data processing : with applications to petroleum prospecting*. CA : Blackwell Scientific Publications, Palo Alto.
- Clouet, J. F. and Fouque, J. P. (1997). A time reversal method for an acoustical pulse propagating in randomly layered media. *Wave Motion*, 25:361–368.
- C. Tsogka and Papanicolaou, G. (2002). Time reversal through a solid-liquid interface and super-resolution. *Submitted to Inverse Problems*.
- Curlander, J. and McDonough, R. (1991). *Synthetic Aperture Radar*. Wiley, New York.
- Devaney, A. Super-resolution processing of multi-static data using time reversal and music. *To appear in J. Acoust. Soc. Am.*

- Dowling, D. R. and Jackson, D. R. (1992). Narrow band performance of phase conjugate arrays in dynamic random media. *J. Acoust. Soc. Am.*, 91:3257–3277.
- Fink, M. (1993). Time reversal mirrors. *J. Phys. D*, 26:1330–1350.
- Fink, M. (1997). Time reversed acoustics. *Phys. Today*, 50:34–40.
- Fink, M., Cassereau, D., Derode, A., Prada, C., Roux, P., and Tanter, M. (2000). Time reversed acoustics. *Rep. Prog. Phys.*, 63:1933–1994.
- Haykin, S., Litva, J., and Shepherd, T. J. (1993). *Radar Array Processing*. Springer-Verlag, New York.
- Kuperman, W. A., Hodgkiss, W. S., Song, H. C., Akal, T., Ferla, C., and Jackson, D. R. (1998). Phase conjugation in the ocean : Experimental demonstration of an acoustic time reversal mirror. *J. Acoust. Soc. Am.*, 103:25–40.
- Papanicolaou, G., Ryzhik, L., and Solna, K. (2002). Statistical stability in time reversal. *Submitted to SIAM J. on Applied Mathematics*.
- Prada, C., Manneville, S., Spolianski, D., and Fink, M. (1996). Decomposition of the time reversal operator: Detection and selective focusing on two scatterers. *J. Acoust. Soc. Am.*, 99:2067–2076.
- Prada, C., Thomas, J. L., and Fink, M. (1995). The iterative time reversal mirror: Analysis of convergance. *J. Acoust. Soc. Am.*, 97:62–71.
- Prada, C., Wu, F., and Fink, M. (1991). The iterative time reversal mirror: A solution to self-focusing in the pulse echo mode. *J. Acoust. Soc. Am.*, 90:1119–1129.
- Schmidt, R. O. (1979). Multiple emitter location and signal parameter estimation. In NY, R. A. D. C. R., editor, *Proc. RADC Spectrum Estimation Workshop*, RADC-TR-79-63, pages 243–258.
- Schmidt, R. O. (1986). Multiple emitter location and signal parameter estimation. *IEEE Trans. Antennas Prop.*, AP-34:276–280.
- Song, H. C., Kuperman, W. A., and Hodgkiss, W. S. (1999). Iterative time reversal in the ocean. *J. Acoust. Soc. Am.*, 105:3176–3184.
- Steinberg, B. (1983). *Microwave Imaging with Large Antenna Arrays*. Wiley, New York.
- Stoica, P. and Moses, R. (1997). *Introduction to Spectral Analysis*. Prentice Hall, New Jersey.
- Tourin, A., Derode, A., Peyre, A., and Fink, M. (2000). Transport parameters for an ultrasonic pulsed wave propagating in a multiple scattering medium. *J. Acoust. Soc. Am.*, 108:503–512.